

RICE UNIVERSITY

**Dynamics of brain networks during reading**

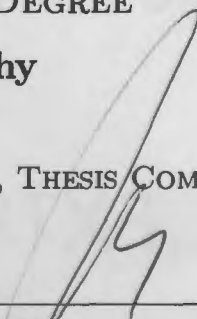
by

**Meagan Lee Whaley**

A THESIS SUBMITTED  
IN PARTIAL FULFILLMENT OF THE  
REQUIREMENTS FOR THE DEGREE

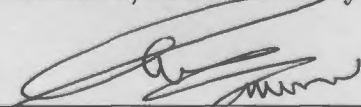
**Doctor of Philosophy**

APPROVED, THESIS COMMITTEE:




---

Steven Cox, Chair  
Professor of Computational and Applied  
Mathematics, Rice University



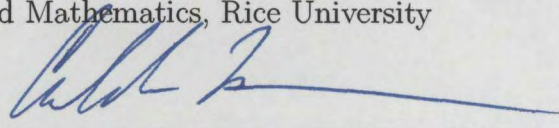
---

Nitin Tandon  
Associate Professor of Neurosurgery, The  
University of Texas Medical School



---

Yuri Dabaghian  
Assistant Professor of Computational and  
Applied Mathematics, Rice University



---

Caleb Kemere  
Assistant Professor of Electrical and  
Computer Engineering, Rice University

Houston, Texas

December, 2015

## ABSTRACT

Dynamics of brain networks during reading

by

Meagan Lee Whaley

We recorded electrocorticographic (ECoG) data from 15 patients with intractable epilepsy during a word completion task to precisely describe the spatiotemporal brain dynamics underlying word reading. Using a novel technique of analyzing grouped ECoG, cortical regions distributed throughout the left hemisphere were identified as significantly active versus baseline during our word stem completion task. Regions of activity spread from fusiform to frontal regions, including pars opercularis, pars triangularis, and pre, post, and subcentral gyri during the time period approaching articulation onset. The ECoG data recorded from electrodes within these regions were fit into linear multivariate autoregressive models, which precisely reveal the time, frequency, and magnitude of information flow between localized brain regions. Grouped network dynamics were quantified with two metrics of evaluating statistical significance of post-stimulus interactions compared to baseline. Results from both methods reveal bidirectional exchanges between frontal regions with fusiform, supporting theories which incorporate top-down and bottom-up processing during single word reading.

# Contents

Abstract	ii
List of Illustrations	v
List of Tables	viii
<b>1 Introduction</b>	<b>1</b>
<b>2 Materials and Methods</b>	<b>6</b>
2.1 Experimental data . . . . .	6
2.2 3D surface representations . . . . .	7
2.3 ECoG collection . . . . .	8
2.4 ECoG processing . . . . .	9
2.5 Surface-based Mixed Effects Multilevel Analysis . . . . .	10
2.6 Time series analysis . . . . .	12
2.7 SdDTF as a measure of network dynamics . . . . .	15
2.8 Two approaches for identifying event-related changes . . . . .	17
2.8.1 Approach 1: Smoothing spline estimates . . . . .	18
2.8.2 Approach 2: statistical testing of post-stimulus, interregional SdDTF values . . . . .	31
2.9 Table of abbreviations for Chapter 2 . . . . .	32
<b>3 Results</b>	<b>34</b>
3.1 SB-MEMA ECoG maps . . . . .	34
3.2 Regional mid-gamma time series . . . . .	36
3.3 Grouped effective connectivity network dynamics . . . . .	39

3.3.1	Flows from fusiform . . . . .	40
3.3.2	Flows from pars opercularis and pars triangularis . . . . .	42
3.3.3	Flows from precentral, postcentral, and subcentral gyri . . . . .	44
<b>4</b>	<b>Discussion</b>	<b>47</b>
4.1	Interactions relative to stimulus onset . . . . .	48
4.2	Interactions relative to articulation onset . . . . .	51
4.3	Limitations . . . . .	55
<b>5</b>	<b>Conclusions</b>	<b>57</b>

## Illustrations

2.1	The 1873 electrodes implanted in all 15 patients are represented on a standard surface. The electrodes in white were viable for our analysis, while those in black were excluded for noise or close proximity to epilepsy tissue. . . . .	8
2.2	Boxplots showing word stem response times for all patients with the median times as the horizontal black bars. RT's with $p < 0.01$ are labeled with red crosses. . . . .	10
2.3	Representational figure of the SdDTF values computed per patient. . . . .	18
2.4	Diagram of the ERC testing framework showing the sequence of steps that were followed for a fixed $f_w$ and electrode pair $(m, n)$ . Every baseline/post-stimulus pair of windows is tested for significance. This diagram excludes the check for $p \leq P$ and $w \leq n_f$ for simplicity. . . . .	29
3.1	Lateral (above) and ventral (below) views of the SB-MEMA maps of post-stimulus percent change from baseline for (left) trials aligned to stimulus onset (0ms) from 50-750ms and (right) RT-aligned trials during the 750ms leading up to RT. The heat map shows significant ( $p=0.01$ , corrected), percent changes from baseline, which is -700ms to -200ms prior to stimulus onset. . . . .	35

3.2	(Left) 183 unique electrodes represented on the N27 surface were situated over the positively activated regions in either panel of Figure 3.1. The number in parenthesis indicates the number of electrodes included per region. (Right) Mean $\pm 1$ SE of percent change in mid gamma power following stimulus onset (above) and leading up to RT (below). The bars at the bottom of each plot indicate times where percent change in power of each region is significantly different from 0 (Wilcoxon signed rank, FDR corrected, $p=0.05$ ). . . . .	37
3.3	ERC flows originating in fusiform. The left column is relative to stimulus onset, and the right column is relative to articulation onset. . . . .	41
3.4	SdDTF flows originating in fusiform. The left column is relative to stimulus onset, and the right column is relative to articulation onset. Red stars indicate time windows that reached significance versus baseline (Wilcoxon signed rank, FDR corrected for $p=0.001$ ). Gray bars show baseline. . . . .	42
3.5	ERC flows to fusiform from regions in the inferior frontal gyrus. The left column is relative to stimulus onset, and the right column is relative to articulation onset. . . . .	43
3.6	SdDTF flows to fusiform from regions in the inferior frontal gyrus. The left column is relative to stimulus onset, and the right column is relative to articulation onset. Red stars indicate time windows that reached significance versus baseline (Wilcoxon signed rank, FDR corrected for $p=0.001$ ). The gray bar shows baseline. . . . .	44
3.7	ERC flows to fusiform from the three regions that border the central sulcus. The left column is relative to stimulus onset, and the right column is relative to articulation onset. . . . .	45

3.8	SdDTF flows to fusiform from the three regions bordering the central sulcus. The left column is relative to stimulus onset, and the right column is relative to articulation onset. Red stars indicate time windows that reached significance versus baseline (Wilcoxon signed rank, FDR corrected for $p=0.001$ ). The gray bar shows baseline. . . . .	46
4.1	ERC flows during three windows following stimulus onset. Top row shows lateral and ventral surfaces, and bottom row shows lateral surface enhanced. Regions are represented by a spheres. The color and width of each arrow is proportional to flow magnitude. . . . .	50
4.2	Significant SdDTF flows during three windows following stimulus onset. Top row shows lateral and ventral surfaces, and bottom row shows lateral surface enhanced. Regions are represented by spheres. The color and width of each arrow is proportional to its flow. . . . .	51
4.3	ERC flows during three windows leading up to articulation onset. Top row shows lateral and ventral surfaces, and bottom row shows lateral surface enhanced. Regions are represented by a spheres. The color and width of each arrow is proportional to flow magnitude. . . . .	54
4.4	Significant SdDTF flows during three windows leading up to articulation onset. Top row shows lateral and ventral surfaces, and bottom row shows lateral surface enhanced. Regions are represented by spheres. The color and width of each arrow is proportional to its flow. . . . .	55

## Tables

2.1	Stimuli for each patient were randomly drawn from this list. . . . .	7
2.2	Patient behavioral data summary. The table shows the total number of trials administered, the number of trials excluded for technical, noisy, or incorrect responses, those excluded with RT's outside 750-2000 ms, and the mean and standard deviation of RT's of the remaining trials. The time between samples of the ECoG recording equipment ( $\Delta t$ in Equation 2.8) is in the last column. . . . .	11
2.3	Table of abbreviations. . . . .	33
3.1	Electrodes organized by patient and region that were analysis with the SdDTF to infer interregional information flow. . . . .	39



# Chapter 1

## Introduction

Reading is an elegant, important part of human interaction. A broad set of regions, situated primarily in the left hemisphere (Price (2012); Fiez and Petersen (1998)), function together to achieve the transformation of visually presented words into spoken output, yet how these regions drive each other is largely unknown. With this research, we set out to address the challenging and clinically important topic of explaining the spatiotemporal dynamics of interregional brain interactions within a specialized set of brain regions during a word reading task with a hybrid analysis of electrocorticographic (ECoG) recordings from 15 humans.

Orthography (visual word representation), semantics (subjective word meaning), and phonology (word sounds) are traditionally accepted as the major processes that give rise to word reading. Studies of language-impaired patients have led to a theory that visual word representations are mapped to their pronunciations through two routes (Patterson and Hodges (1992); McCarthy and Warrington (1986); Coltheart et al. (1993)): the direct route (which maps words directly to their meanings); and the indirect route (which maps words directly to their sounds). The routes operate interactively and in parallel with one another (Dehaene (2009, Chapter 1, pages 40-41)). Where these routes are anatomically realized (if they do indeed exist) is a matter of continued interest (Jobard et al. (2003)).

The Connectionist model (Seidenberg (2005)) provides an alternate framework where

word reading is achieved through multi-layered, weighted links connecting orthographic, phonological, and semantic units. The weights adjust as the network learns how to generate the correct pronunciation for each input. Neither the Dual-Route nor Connectionist models make predictions at the neural level. Additionally, empirical support for the models (Jobard et al. (2003)) often include regions that perform multiple functions, adding to the difficulty of validating the models (Mechelli et al. (2005)).

Perhaps the most illustrious anatomical region associated with word reading is a location in the sulcus at the junction of ventral occipital and temporal cortices (referred to as the occipitotemporal junction (vOT)). This area, referred to by some as the Visual Word Form Area (Dehaene and Cohen (2011)), responds to multimodal inputs with preferential robust activations for word and word-like stimuli within the first several hundred milliseconds following stimulus onset. While debate has surrounded the functional specificity of the vOT, (Price and Devlin (2003)), it is undeniably an area of remarkable interest.

The Interactive Account hypothesizes (Price and Devlin (2011)) that vOT is involved in dynamic feedforward and feedback interactions with “sensory and higher level regions.” These connections enable the reading network to achieve accurate performance by integrating top-down predictions (gained from experience) with bottom-up visual information. A clear anatomical prediction made by the Interactive Account is that bottom-up, feedforward transmissions from vOT will exceed top-down processes for unfamiliar visual input, such as pronounceable, meaningless letter strings or unfamiliar words. Recent evidence (Schurz et al. (2014); Carreiras et al. (2014)) has supported the plausibility of the Interactive Account, yet

the time course of interactions involving vOT has yet (to our knowledge) been investigated with ECoG.

With this work, we sought to understand how the area associated with pre-lexical processing engages the rest of the word reading network, thus testing the validity of the Interactive Account.

Owing to its exceptional temporal and spatial resolution, ECoG is especially well-suited for characterizing the fast neural activation patterns during language tasks (Nobre et al. (1994); Mainy et al. (2008); Lachaux et al. (2012)). Broad gamma (approximately 30-240Hz) ECoG activity has proven to be a robust task-specific indicator in a number of language and memory tasks (Crone et al. (2001b); Lachaux et al. (2012); Edwards et al. (2010); Conner et al. (2014); Kadipasaoglu et al. (2014)). Continuing in the spirit of a recent electroencephalogram (EEG) study (Bedo et al. (2014)), we have pursued the goal of determining how regions communicate during word reading, with a particular focus on the fusiform (which is near vOT), utilizing precise maps of brain dynamics inferred from ECoG data within the mid gamma (60-120Hz) range.

Approaches to achieve this goal include Granger Causality (Granger (1969); Brovelli et al. (2004)), the directed transfer function (Kamiński and Blinowska (1991)), and Amplitude Envelope Correlation (Vidal et al. (2012); Conner et al.). Korzeniewska et al. (2008) combined two methods, partial coherence and the directed transfer function, when they introduced the Short-time direct Directed Transfer Function (SdDTF) within the statistical testing framework of the Event-Related Causality (ERC) method. SdDTF values indicate directionality,

that is, whether a region is sending or receiving information, and connectivity, whether the flows are direct or mediated by another region, over a desired frequency range, thus providing concise descriptions of network dynamics. It is a powerful statistical tool that treats multiple time series as a single, multivariate system, rather than piecing together individual or bivariate components into a global model. This multidimensional design appeals to our investigation of widespread regions across the left hemisphere. Its demonstrated ability to reveal meaningful conclusions from individual (Korzeniewska et al. (2008), Korzeniewska et al. (2011)) and grouped ECoG (Flinker et al. (2015)) motivated us to extend this method to discover patterns at the group level from our word stem completion ECoG data.

During our word stem completion task, we collected ECoG data from 15 patients as they viewed a series of partial words (stems), e.g., “ru\_”. Each patient was instructed to say aloud the first action word that came to mind (“running”). We worked under the assumption that word stem completion and word reading involve similar processes, with the difference that word retrieval time is slower during word stem completion (Dhond et al. (2001)). In addition to support from neuroimaging evidence (Ojemann et al. (1998)), we confirmed that the brain locations significantly active during our word stem task (which include fusiform, pars triangularis, pars opercularis, precentral, subcentral, and postcentral) largely agree with word reading networks identified by both fMRI (Price (2012)) and ECoG (Vidal et al. (2012)) and category-specific networks (Conner et al. (2014)), leading us to conclude that similar processes are indeed recruited during both tasks.

Our grouped network analysis revealed fusiform holds dynamic conversations with pars

triangularis, pars opercularis, precentral, postcentral, and subcentral regions. Fusiform remains online from stimulus onset through articulation onset, sending and receiving flows from areas associated with semantic and phonological processing. Taken together, the dynamic, time-varying bi-directional links fit better within the Connectionist framework (and particularly the Interactive account from Price and Devlin (2011)) than the Dual-Route framework.

In the sections to follow, we elaborate on the details of how we achieved our findings, starting with the experimental ECoG data in §§2.1, 2.3, and 2.4. The pre- and post-operative image acquisition specifications are given in §2.2. The grouped ECoG analysis technique is discussed next in §2.5, followed by the time series methods used to model the ECoG data in §2.6 and the SdDTF measure of information flow in §2.7. The statistical framework we utilized is covered in Section 2.8. Chapter 3 gives the grouped ECoG results in §3.1, regional mid-gamma activations in §3.2, and concludes with dynamics of regional interactions inferred from ERC in §3.3. We discuss their relevance to describing the nature of word reading in Chapter 4, offering our final remarks and conclusions in Chapter 5.

## Chapter 2

### Materials and Methods

We collected ECoG from fifteen patients with intractable epilepsy (5 male; mean  $32 \pm 10$  years; average IQ of  $97 \pm 13$ ; 1 left-handed) who underwent surgical implantation of subdural electrodes for seizure localization. Following approval by the University of Texas Health Science Center's committee for protection of human subjects, informed consent was obtained from all patients to participate in this study.

#### 2.1 Experimental data

Several days after their electrode implantation surgeries, patients performed a series of language tasks, including word stem completion. During word stem, patients viewed 80-100 stimuli on a 15" LCD monitor presented at eye level approximately 2 feet away. Stimuli consisted of black, lower-case text (font height of 100 pixels, font type of Calibri) on a  $1300 \times 800$  pixel white background. Patients were instructed to complete each stem with the first action word that came to mind. Stimuli were randomly drawn from the list in Table 2.1.

The transistor-transistor logic pulse initialized by the task presentation software recorded the time of stimulus onset. The audio recording of each task session was used to label the onset of articulation and measure the reaction time, RT.

avoi	bak	ben	blen	boi	brea	bru	brus	bu	buil
cal	catc	chas	che	cho	clea	cli	clim	coun	craw
danc	div	dra	drea	dres	drin	driv	dum	ea	eras
fal	fee	fl	giv	gro	hea	hel	hol	hun	jum
kee	kis	knee	knoc	lau	lea	lear	lis	loo	lov
mov	pai	pla	pou	pra	prac	punc	pus	qui	rea
reac	rid	ru	se	shak	sho	si	slee	smil	smok
spea	stan	stea	sto	stretc	swi	tak	thro	tou	tur
visi	wast	wav	wea	wor	wri				

Table 2.1 : Stimuli for each patient were randomly drawn from this list.

## 2.2 3D surface representations

Prior to implantation surgery, a 3T whole-body MR scanner (Philips Medical Systems, Bothell WA) furnished with a 16-electrode SENSE head coil was used to collect the anatomical MRI scans with magnetization-prepared 180 degree radio-frequency pulses and rapid gradient-echo (MP-RATE) sequence. The scanner was optimized for gray-white matter contrast with 1 mm thick sagittal slices and an in-plane resolution of  $0.938 \times 0.938$  (Ellmore et al. (2009)). Following the scans, the cortical surface representations were reconstructed with FreeSurfer software (v5.1) (Dale et al. (1999)) which were then imported to SUMA (Saad and Reynolds (2012)) for our analysis.

### 2.3 ECoG collection

1873 total subdural electrodes (PMT Corporation; top-hat design; 3 mm diameter contact with cortex) were implanted following methods previously published (Tandon (2008)). Figure 2.1 shows all electrodes implanted represented on a standard N27 surface. Those in white were viable for our analysis, and those in black were excluded due to noise or close proximity to epilepsy tissue.

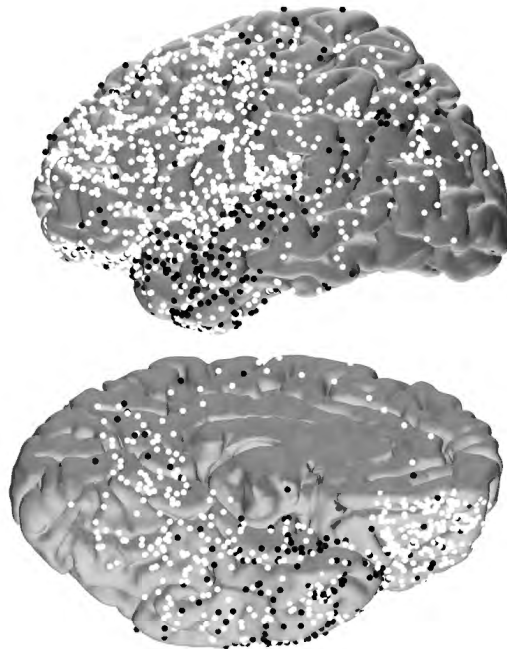


Figure 2.1 : The 1873 electrodes implanted in all 15 patients are represented on a standard surface. The electrodes in white were viable for our analysis, while those in black were excluded for noise or close proximity to epilepsy tissue.

The ECoG data was collected at 1000 Hz using NeuroFax software (Nihon Kohden,

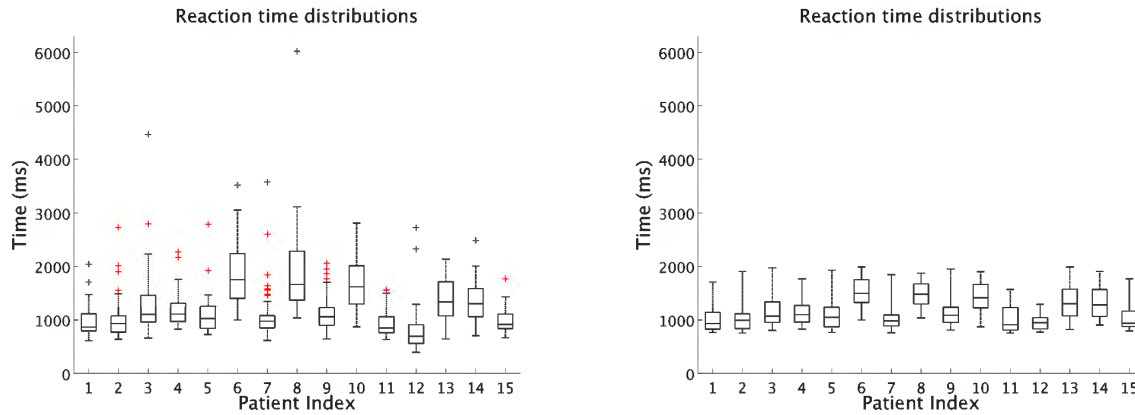


Tokyo, Japan,  $\Delta t = 1\text{ms}$  in Table 2.2) with a bandwidth of 0.15-300Hz or at 2000Hz using NeuroPort NSP (Blackrock Microsystems, Salt Lake City, UT,  $\Delta t = 0.5\text{ms}$  in Table 2.2) with a bandwidth of 0.1-750Hz (see Table 2.2 for the breakdown by patient). The data from every electrode was re-referenced to a common average which excluded those with 60Hz noise or interictal activity when initially referenced to an artificial 0V (Crone et al. (2001a)). Electrodes were localized following previously published techniques in Pieters et al. (2013). 436 were excluded due to 60Hz noise or epileptiform activity. Of the remaining electrodes, a subset of 183 electrodes was selected for the network analysis based on the SB-MEMA analysis.

## 2.4 ECoG processing

Patients' videos were reviewed to exclude trials with unclear or incorrect responses. Additionally, trials with epileptiform activity or 60Hz noise were excluded. The distribution of each patient's RT's over the remaining trials are presented in Figure 2.2a, with outliers ( $p < 0.01$ ) shown as red crosses.

The time from stimulus offset to the next stimulus onset randomly varied between XXX and 8.5 s. With the aim of creating grouped, time evolving activation maps describing word reading networks, trials with response times outside the 750-2000 ms window after stimulus onset were excluded (see Figure 2.2b for the distributions of RT for the remaining trials). Furthermore, we analyzed time periods for trials aligned to stimulus onset and to RT to capture the collective cognitive processes engaged by all patients after viewing the stimulus



(a) Distribution of all RT's.

(b) RT distribution after excluding trials.

Figure 2.2 : Boxplots showing word stem response times for all patients with the median times as the horizontal black bars. RT's with  $p < 0.01$  are labeled with red crosses.

and during the period leading up to articulation onset.

Table 2.2 summarizes patient behavioral data, including the total trials presented and the number removed for incorrectness or noise (lumped into the Excluded trials column) or RT. The mean and standard deviation (St Dev) of RT for the remaining trials is shown, as well as the time between samples for the ECoG recordings in the last column ( $\Delta t$  in Equation (2.8)).

## 2.5 Surface-based Mixed Effects Multilevel Analysis

To achieve statistically robust and topologically accurate analyses of individual and population-level ECoG data, we implemented a surface-based mixed-effects multilevel analysis (SB-

Patient	Total trials	Excluded trials	RT<750ms or RT>2000ms	Remaining trials	Mean RT (ms)	St Dev RT (ms)	$\Delta t$ (ms)
1	80	39	9	32	1027	263	1
2	80	27	11	42	1027	254	1
3	80	35	6	39	1175	310	1
4	80	34	2	44	1138	205	1
5	80	46	3	31	1062	263	1
6	80	23	19	38	1519	259	1
7	80	19	9	52	1055	256	1
8	80	33	15	32	1486	228	1
9	80	31	6	43	1149	280	1
10	80	48	8	24	1451	289	0.5
11	100	67	7	26	1022	275	0.5
12	100	46	34	20	973	173	0.5
13	100	64	6	30	1340	315	0.5
14	80	27	3	50	1311	282	1
15	100	67	4	29	1045	258	0.5

Table 2.2 : Patient behavioral data summary. The table shows the total number of trials administered, the number of trials excluded for technical, noisy, or incorrect responses, those excluded with RT's outside 750-2000 ms, and the mean and standard deviation of RT's of the remaining trials. The time between samples of the ECoG recording equipment ( $\Delta t$  in Equation 2.8) is in the last column.

MEMA) (Kadipasaoglu et al. (2014)). SB-MEMA was developed to overcome challenges in grouped ECoG analyses due to: a) individual data representation - arising from difficulties in the accurate localization and spatial transformation of ECoG on convoluted cortical topology (Miller et al. (2007); Dykstra et al. (2012); Esposito et al. (2012); Conner et al. (2014)); b) inter-subject comparisons - arising from issues of sparse sampling and inter-subject anatomical variability (Lachaux et al. (2003); Anticevic et al. (2008); Jerbi et al. (2009); Oosterhof et al. (2011); Saad and Reynolds (2012)); and finally c) statistical analyses of grouped datasets - arising from small sample sizes, missing data, and violations in the

assumptions of traditional statistical models (e.g. ANOVA/t-tests) (Chen et al. (2012); Conner et al. (2014); Kadipasaoglu et al. (2014)). To address these issues, we developed novel methods to accurately represent recording electrode coverage sites and spatially transform high-frequency ECoG activity on cortical surface models. We integrated these techniques with surface-based co-registration to correct for inter-subject anatomical variability, and have incorporated a mixed-effects multilevel grouped analysis to control for sparse sampling, outlier inferences, as well as intra-and inter-subject variability (Kadipasaoglu et al. (2014)). In sum, SB-MEMA yields increased statistical power and more accurate grouped effect estimates to enable the generation of multi-human brain activity maps of cognitive functions, such as reading, that are impossible to study save in humans.

## 2.6 Time series analysis

For a single patient, the electrical potential recordings from each electrode during the word stem task generate time series with  $N_s$  values per trial, which refers to the time between stimulus onsets. After bandpass filtering the ECoG for 60 Hz noise (using a square filter with sigmoid flanks and half amplitude roll off of 1.5 Hz), the ECoG data was divided into trials, which were aligned to stimulus onset or RT and split into  $n_\tau$  windows of length  $n_s$ . The trial mean was subtracted from the data at every time point before dividing by the trial standard deviation. Then, within each window, the (window) temporal mean was subtracted from the entire trial before dividing by the (window) temporal standard deviation. For  $n_t$  total trials, the resulting pre-processed signal from electrode  $i$  is  $x^i \in \mathbb{R}^{N_s \times n_t}$ . The  $n_e$  electrode signals

identified with SB-MEMA for a single patient and fixed time  $j$  and trial  $k$  are organized together in  $X_{j,k} = \{x_{j,k}^1, x_{j,k}^2, \dots, x_{j,k}^{n_e}\} \in \mathbb{R}^{n_e}$ .

For a fixed trial  $k$ , the patient-specific multivariate time series are fit to the predictive Multivariate Autoregressive (MVAR) model on each window

$$X_{j,k} + \sum_{\ell=1}^m A_{\ell}^{(m)} X_{j-\ell,k} = E_{j,k}^{(m)}. \quad (2.1)$$

The model of (2.1) encodes multivariate causality in the entries of the unknown convolution matrices  $A_{\ell}^{(m)} \in \mathbb{R}^{n_e \times n_e}$ , which include information from *every* electrode. The model order  $m$ , selected as the minimizer of Equation 2.4, gives the number of time points in the past used to forecast the time series at time  $j$ . The unknown convolution matrices and model fit error term,  $E_{j,k}^{(m)} \in \mathbb{R}^{n_e}$ , are retrievable with certain assumptions on  $X$  and  $E$ .

Firstly,  $X$  and  $E$  are assumed to have zero-mean, which is guaranteed during pre-processing. Next, we presume that  $X$  is weakly stationary and weakly ergodic. A key property of a weakly stationary  $X$  is that its lagged trial averages (called lagged cross-correlation matrices) only depend upon the time shift. This dependence is seen in the definition of the cross-correlation matrix of lag  $u$  in

$$R_u \equiv \frac{1}{n_t} \sum_{k=1}^{n_t} X_{j,k} X_{j+u,k}^T, \quad 1 \leq j \leq n_s - u.$$

Furthermore, when we are permitted to exchange the (trial-averaged) cross-correlation with the (time-averaged) cross-correlation from a single trial,

$$R_u = \frac{1}{n_s - u} \sum_{j=1}^{n_s - u} X_{j,k} X_{j+u,k}^T,$$

$X$  is weakly ergodic (Bendat and Piersol (1971, §3.3)). Finally, we presume that the model error is uncorrelated with the time series at all non-zero lags, so that for model order  $m$ ,

$$\sum_j^{n_t} E_{j,k}^{(m)} X_{j-\ell,k}^T = 0, \quad \ell > 0.$$

Under these standard assumptions, we take the outer product of  $X_{j-\ell,k}^T$  with the model in (2.1) and upon taking averages, arrive at

$$R_{-u} + A_1 R_{-u+1} + \dots + A_m R_{-u+m} = 0, \quad u = 1, \dots, m, \quad (2.2)$$

the Yule-Walker Equations (Ding et al. (2006, Chapter 17)). With the assumption of weak ergodicity, the empirical cross-correlations are computed and trial-averaged

$$R_u = \frac{1}{n_t} \sum_{k=1}^{n_t} \left( \frac{1}{n_s - u} \sum_{j=1}^{n_s - u} X_{j,k} X_{j+u,k}^T \right).$$

Given  $m$ ,  $\{A_1^{(m)}, \dots, A_m^{(m)}\}$  are determined using Equation (2.2) with the method presented in Morf et al. (1978). The model order  $m$  is selected as the minimizer which reduces error related to  $C^{(m)}$ , the time-independent covariance matrix of  $E_i^{(m)}$ , while penalizing for over-fitting with large orders. An expression for computing  $C^{(m)}$  is obtained by right-multiplying Equation (2.1) with  $X_{j,k}^T$  and averaging

$$C^{(m)} = R_0 + \sum_{\ell=1}^m A_\ell^{(m)} R_\ell. \quad (2.3)$$

With all the supporting definitions in place, the model order  $m$  is now formally defined as the minimizer of the Bayesian Information Criterion, or *BIC* (Ding et al. (2006, Chapter 17)),

$$BIC(m) = 2 \log(\det(C^{(m)})) + (2n_e^2 m \log(n_s n_t)) / n_s n_t. \quad (2.4)$$

Once the model order is chosen, the superscript notation is dropped.

## 2.7 SdDTF as a measure of network dynamics

The MVAR model in (2.1) allows for a smooth transition to frequency domain representations of information transfer and connectivity, including the (directed) transfer function and partial coherence ( $H$  and  $P$ , respectively). Combining these measures yields the Short-time Direct Directed Transfer Function, (SdDTF), a measure of direct, directed information flow. Upon selecting the model order  $m$  as the minimizer of Equation 2.4 (and subsequently dropping it from the superscript notation), the MVAR model in (2.1) is rearranged

$$\sum_{\ell=0}^m A_{\ell} X_{j-\ell,k} = E_{j,k}. \quad (2.5)$$

where  $A_0 = I_{n_e \times n_e}$ , the  $n_e \times n_e$  identity matrix. For arbitrary time series  $S \in \mathbb{R}^K$  defined on the grid  $t_k = k\Delta t$ ,  $k = 0, \dots, K-1$ , for the time constant  $\Delta t$ , the discrete Fourier transform at frequency  $f_w$  (Bendat and Piersol (1971, §9.3.2)) is

$$\hat{S}_w = \sum_{k=0}^{K-1} S_n \exp(-2\pi i f_w k \Delta t). \quad (2.6)$$

For this  $\Delta t$ , frequencies up to  $1/2\Delta t$  (the Nyquist frequency) are well-defined (Bendat and Piersol (1971, §7.3.1)).  $\Delta t$  is experimentally constrained because it depends on the time between samples of the ECoG recordings (see Table 2.2) and is at most 1 ms, giving a Nyquist frequency of 500 Hz. Frequency indices  $w = 1, \dots, n_f$  match frequency values  $f_1, \dots, f_{n_f}$ , and for our analysis,  $f_w = w\Delta w$ ,  $\Delta w = 2$  Hz. We focused on the mid-gamma frequency range, so  $60 \text{ Hz} \leq f_w \leq 120 \text{ Hz}$ .

Applying the discrete Fourier Transform of (2.6) to the model in (2.5) allows us to retrieve

spectral information of the  $k^{th}$  trial

$$\hat{X}_{w,k} = H_w \hat{E}_{w,k}. \quad (2.7)$$

$\hat{X}$  is the Fourier transform of  $X$ ,  $\hat{E}$  is the Fourier transform of  $E$ , and the (directed) transfer function

$$H_w = \left( \sum_{\ell=0}^m A_\ell \exp(-2\pi i f_w \ell \Delta t) \right)^{-1} \quad (2.8)$$

is the inverse of the Fourier transform of the  $A$  matrices. A nonzero value at the  $(i, j)^{th}$  index,  $H_w(i, j)$ , suggests the presence of a flow from electrode  $j$  to electrode  $i$  at frequency  $f_w$ , although the flow may not necessarily be direct.

Right multiplying Equation 2.6 by  $\hat{X}_{w,k}^*$  and trial-averaging gives the formula used to compute the spectral matrix of  $X$

$$S_w = H_w C H_w^*. \quad (2.9)$$

Let  $\rho_w(m, n)$  denote the  $(m, n)^{th}$  element of  $S_w^{-1}$ . The particle coherence function is constructed entry-wise

$$\gamma_w(m, n) = \frac{\rho_w(m, n)}{\sqrt{\rho_w(m, m)\rho_w(n, n)}}. \quad (2.10)$$

A nonzero partial coherence value at frequency index  $w$  and electrode index  $(i, j)$  suggests a direct connection between electrodes  $i$  and  $j$  at frequency  $f_w$ .  $\gamma$  is symmetric and therefore does not encode directionality of flow between electrodes.

$H$  and  $\gamma$  are combined with their entry-wise normalized products with the SdDTF. The SdDTF value between the  $m^{th}$  and  $n^{th}$  time series is

$$G_w(m, n) = \frac{|H_w(m, n)| |\gamma_w(m, n)|}{\sqrt{\sum_{w=1}^{n_f} \sum_{(k,l) \in J_{n_e}} |H_w(k, l)|^2 |\gamma_w(k, l)|^2}}, \quad (2.11)$$



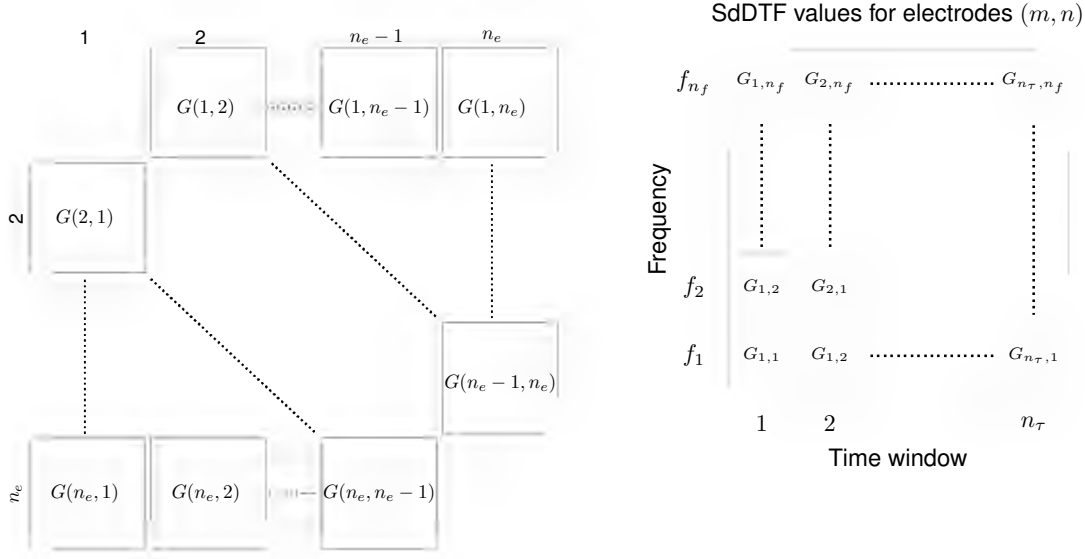
$$J_{n_e} = \{(1, 2), (1, 3), \dots, (1, n_e), (2, 1), (2, 3), \dots, (2, n_e), \dots, (n_e, 1), (n_e, 2), \dots, (n_e, n_e - 1)\}.$$

For electrodes  $m$  and  $n$  on the window  $\tau_i$  ( $1 \leq i \leq n_\tau$ ) at frequency  $f_w$ , the SdDTF value is denoted  $G_{i,w}(m, n)$ , so  $G_{.,.}(m, n) \in \mathbb{R}^{n_f \times n_\tau}$ . A nonzero SdDTF value suggests a direct flow from electrode  $n$  to electrode  $m$  at frequency  $f_w$  during window  $\tau_i$ . Thus, we have a clear quantification of the precise time, frequency, direction, and magnitude of information flow between brain regions of interest for each patient.

When referring to the time/frequency values of  $G$  for a fixed electrode pair, we drop its notation so  $G_{i,w}(m, n) = G_{i,w}$ . Figure 2.3 gives representational diagrams of the range of SdDTF values (and notation) for a single patient showing how the function is evaluated for all electrode pairs (with frequency/time window notation dropped in 2.3a) and time/frequency values for fixed electrode pair (with electrode number notation excluded in 2.3b).

## 2.8 Two approaches for identifying event-related changes

Statistical significance of post-stimulus SdDTF values was evaluated with two approaches. The discussion on the Event-related causality (ERC) technique, which was originally developed as a method for identifying post-stimulus windows where smoothed SdDTF values significantly differ from baseline (Korzeniewska et al. (2008, 2011)) is given in §2.8.1. In §2.8.2, we present a different approach which we adapted to evaluate significance directly from the SdDTF values averaged by region. This approach allows for a more direct comparison of interregional baseline flows with post-stimulus flows.



(a) SdDTF values are computed for each pair of electrodes.

(b) SdDTF values are computed over time and frequency for fixed electrode pair (one square of Figure 2.3a).

Figure 2.3 : Representational figure of the SdDTF values computed per patient.

### 2.8.1 Approach 1: Smoothing spline estimates

ERC requires statistical information about the SdDTF values to test for significance. These measures can be estimated through bootstrapping or a different, computationally efficient approach of smoothing functions (Wang and Wahba (1994)). As such, the SdDTF observations  $G$  (Wahba and Wendelberger (1980); Korzeniewska et al. (2008)) were refined with the smoothing function  $s : \mathbb{R}^2 \mapsto \mathbb{R}$  that is related to the SdDTF values through

$$G_{i,w} = s_{i,w} + e_{i,w}, \quad e_{i,w} \sim N(0, \sigma^2), \quad (2.12)$$

where the subscripted indices refer to point-wise evaluation at the corresponding time/frequency  $((i, w)$  corresponds to  $(\tau_i, f_w)$ , in this case).  $s$  is chosen as the function which minimizes  $\phi$

$$\phi(s) \equiv \frac{1}{n_f n_\tau} \sum_{w=1}^{n_f} \sum_{i=1}^{n_\tau} (s_{i,w} - G_{i,w})^2 + \lambda P(s), \quad \lambda > 0 \quad (2.13)$$

where  $P$  is the penalty function

$$P(q) = \int_{-\infty}^{\infty} \int_{-\infty}^{\infty} \left( \left( \frac{\partial^2 q}{\partial u^2} \right)^2 + 2 \left( \frac{\partial^2 q}{\partial u \partial \nu} \right)^2 + \left( \frac{\partial^2 q}{\partial \nu^2} \right)^2 \right) du d\nu. \quad (2.14)$$

$\phi$  strikes a balance between finding a function which fits the data well while penalizing for roughness. We work toward giving the well-known solution to this problem by first reindexing our domain to simplify notation. Let  $M = n_\tau n_f$  and define  $d_i \equiv (\tau_{\text{ceil}(i/n_f)}, f_{i - n_f \text{floor}(i/n_f)})$ ,  $i = 1, \dots, M$ . With this convention,  $d_1 = (\tau_1, f_1)$ ,  $d_2 = (\tau_1, f_2)$ ,  $\dots$ ,  $d_M = (\tau_{n_\tau}, f_{n_f})$ .

For any  $u, \nu \in \mathbb{R}^2$ , let

$$\psi(u, \nu) = \frac{1}{8\pi} \|u - \nu\|^2 \log(\|u - \nu\|) = \frac{1}{16\pi} \|u - \nu\|^2 \log(\|u - \nu\|^2).$$

From  $\psi$ , define  $Z \in \mathbb{R}^{M \times M}$  by its  $(i, j)^{\text{th}}$  element,  $Z(i, j) = \psi(d_i, d_j)$ . Form the vector  $g \in \mathbb{R}^M$  from the SdDTF values,  $g_i = G_{d_i}$ , and define the matrix  $D \in \mathbb{R}^{M \times 3}$  from the points on our domain

$$D = \begin{pmatrix} \begin{pmatrix} 1 & 1 & \dots & 1 \end{pmatrix}_{1 \times n_f} & \begin{pmatrix} 1 & 1 & \dots & 1 \end{pmatrix}_{1 \times n_f} & \dots & \begin{pmatrix} 1 & 1 & \dots & 1 \end{pmatrix}_{1 \times n_f} \\ \begin{pmatrix} \tau_1 & \tau_1 & \dots & \tau_1 \end{pmatrix}_{1 \times n_f} & \begin{pmatrix} \tau_2 & \tau_2 & \dots & \tau_2 \end{pmatrix}_{1 \times n_f} & \dots & \begin{pmatrix} \tau_{n_\tau} & \tau_{n_\tau} & \dots & \tau_{n_\tau} \end{pmatrix}_{1 \times n_f} \\ \begin{pmatrix} f_1 & f_1 & \dots & f_{n_f} \end{pmatrix}_{1 \times n_f} & \begin{pmatrix} f_1 & f_1 & \dots & f_{n_f} \end{pmatrix}_{1 \times n_f} & \dots & \begin{pmatrix} f_1 & f_1 & \dots & f_{n_f} \end{pmatrix}_{1 \times n_f} \end{pmatrix}^T$$

**Proposition 1** *If  $\text{Null}(D) = \{0\}$ , then,  $\phi$  has a unique minimizer on the domain  $\{d_1, d_2, \dots, d_M\}$  over an appropriately defined Hilbert space for which  $P(s)$  is finite. The minimizer  $s$  takes*

the form (Wahba and Wendelberger (1980))

$$s_u = \sum_{i=1}^M \alpha_i \psi(u, d_i) + \beta_1 + \beta_2 u_1 + \beta_3 u_2. \quad (2.15)$$

The unknown weights  $\alpha_i$  and  $\beta_i$  obey

$$\begin{pmatrix} Z + \lambda M I_{M \times M} & D \\ & D^T & 0_{3 \times 3} \end{pmatrix} \begin{pmatrix} \alpha \\ \beta \end{pmatrix} = \begin{pmatrix} g \\ 0_{3 \times 1} \end{pmatrix} \quad (2.16)$$

To show how the splines were determined in practice (Green and Silverman (1994, §8.2.1)), begin with the QR decomposition of  $D = QR$  for orthogonal  $Q \in \mathbb{R}^{M \times M}$  and upper triangular  $R \in \mathbb{R}^{M \times M}$ . Next partition  $Q$  and  $R$  as

$$D = \begin{pmatrix} Q_1 & Q_2 \end{pmatrix} \begin{pmatrix} R_1 \\ R_2 \end{pmatrix},$$

where  $Q_1 \in \mathbb{R}^{M \times 3}$ ,  $Q_2 \in \mathbb{R}^{M \times (M-3)}$ ,  $R_1 \in \mathbb{R}^{3 \times 3}$ , and  $R_2 = 0_{(M-3) \times 3}$ . Presuming  $D$  is full rank,  $R_1$  is invertible. Rewrite the non-zero portion of  $D^T \alpha = 0$  in terms of its QR-decomposition

$$R_1^T Q_1^T \alpha = 0.$$

From the invertibility of  $R_1$  and the orthogonality of  $Q_1$  and  $Q_2$ , we conclude there is some  $\nu \in \mathbb{R}^{(M-3)}$  such that

$$\alpha = Q_2 \nu. \quad (2.17)$$

Next, left-multiply  $(Z + \lambda M I_{M \times M})\alpha + D\beta = g$  by  $Q_1^T$  to determine a simplified expression for  $\beta$ ,

$$Q_1^T (Z + \lambda M I_{M \times M})\alpha + Q_1^T Q_1 R_1 \beta = Q_1^T g.$$

Substituting  $\alpha = Q_2\nu$  and using orthogonality of  $Q_1$  and  $Q_2$ , we arrive at

$$Q_1^T Z Q_2 \nu + R_1 \beta = Q_1^T g.$$

Solving for  $\beta$  gives

$$\beta = R_1^{-1} (Q_1^T g - Q_1^T Z Q_2 \nu). \quad (2.18)$$

A cleaner expression for the unknown  $\nu$  is determined by again left-multiplying but this time with  $Q_2^T$  to determine an expression for the unknown  $\nu$ ,

$$(Q_2^T Z Q_2 + \lambda M I_{K \times K}) \nu = Q_2^T g. \quad (2.19)$$

Determine the Cholesky decomposition,  $Q_2^T Z Q_2 = LL^T$ , where  $L \in \mathbb{R}^{(M-3) \times (M-3)}$  is lower triangular, and the Singular Value Decomposition,  $L = U \Sigma V^T$ , with unitary matrices  $U, V \in \mathbb{R}^{(M-3) \times (M-3)}$  and diagonal matrix  $\Sigma \in \mathbb{R}^{(M-3) \times (M-3)}$ . Then

$$Q_2^T Z Q_2 = U \Sigma \Sigma U^T. \quad (2.20)$$

Substituting these decompositions into Equation (2.19) gives

$$\nu = U (\Sigma \Sigma + \lambda M I_{(M-3) \times (M-3)})^{-1} U^T Q_2^T g. \quad (2.21)$$

Computing  $\nu$  then requires the inverse of the diagonal matrix  $(\Sigma \Sigma + \lambda I_{(M-3) \times (M-3)})$ , which is computationally inexpensive. From  $\nu$ ,  $\alpha$  is obtained from Equation (2.17). Finally,  $\beta$  is computed from Equation (2.18), which requires solving a lower triangular system.

For arbitrary, fixed  $\lambda$ , the pieces are in place to compute the thin plate spline estimates for our data observations. We now resolve how  $\lambda$  was selected in practice using generalized

cross validation, or GCV (Green and Silverman (1994, §§3.2, 8.2.1)). The goal of GCV is to select the parameter  $\lambda$  which yields the spline with the best predictive power measured in terms of the sum of squared error over reduced sets of data.

Begin by fixing index  $i$  and removing one observation  $G_{d_i}$  and its corresponding time-frequency location  $d_i$  from the set of total observations and the domain. The thin plate spline computed over this reduced set of data is denoted  $s^{(\lambda, -d_i)}$ . Ideally,  $s_{d_i}^{(\lambda, -d_i)}$  will be a “good” predictor of  $G_{d_i}$  in the sense that the squared difference

$$\left( s_{d_i}^{(\lambda, -d_i)} - G_{d_i} \right)^2$$

is minimal.

For a fixed  $\lambda$ , presume there is a matrix  $V^{(\lambda)} \in \mathbb{R}^{M \times M}$  such that

$$\begin{pmatrix} s_{d_1}^{(\lambda)} & s_{d_2}^{(\lambda)} & \dots & s_{d_M}^{(\lambda)} \end{pmatrix}^T = V^{(\lambda)} g \quad (2.22)$$

Then the generalized cross validation score for  $s^{(\lambda)}$ ,  $GCV(s, \lambda)$ , is the weighted average of the predictive errors

$$GCV(s, \lambda) \equiv \frac{1}{M} \sum_{i=1}^M \left( \frac{1 - V^\lambda(i, i)}{1 - M^{-1} \text{trace}(V^{(\lambda)})} \right)^2 (G_{d_i} - s_{d_i}^{(\lambda, -d_i)})^2. \quad (2.23)$$

Notice that Equation (2.23) calls for the computation  $V^{(\lambda)}$  in addition to the  $M$  splines for each reduced set of data for a total of  $M + 1$  splines. Now, it will be shown how to determine an equivalent formulation for  $GCV(s, \lambda)$  that requires significantly reduced number of splines. For a fixed  $i$  and  $1 \leq j \leq M$ , construct the vector  $t \in \mathbb{R}^M$

$$t_j = \begin{cases} G_{d_j} & j \neq i \\ s_{d_i}^{(\lambda, -d_i)} & \text{if } j = i \end{cases}.$$

Then (by Lemma 3.1 in Green and Silverman (1994)),

$$\begin{pmatrix} s_{d_1}^{(\lambda, -d_i)} & s_{d_2}^{(\lambda, -d_i)} & \dots & s_{d_M}^{(\lambda, -d_i)} \end{pmatrix}^T = V^{(\lambda)} t.$$

To reformulate the *GCV*, we expand the product of the  $i^{\text{th}}$  row of  $V^{(\lambda)}$  with  $t$ , and along with the definition of  $t$ , we see that

$$\begin{aligned} V^{(\lambda)}(i, :)t &= \sum_{j \neq i} V^{(\lambda)}(i, j)t_j + V^{(\lambda)}(i, i)t_i \\ &= \sum_{j \neq i} V^{(\lambda)}(i, j)G_{d_j} + V^{(\lambda)}(i, i)s_{d_i}^{(\lambda, -d_i)} \end{aligned}$$

Adding and subtracting  $V^{(\lambda)}(i, i)G_{d_i}$  and gathering terms gives

$$V^{(\lambda)}(i, :)t = V^{(\lambda)}(i, :)g + V^{(\lambda)}(i, i)(s_{d_i}^{(\lambda, -d_i)} - G_{d_i}).$$

Use Equation (2.22) for  $V^{(\lambda)}(i, :)g$  to see that

$$V^{(\lambda)}(i, :)t = s_{d_i}^{(\lambda)} + V^{(\lambda)}(i, i)(s_{d_i}^{(\lambda, -d_i)} - G_{d_i}).$$

Then the difference in the numerator of Equation 2.23 is

$$\begin{aligned} G_{d_i} - s_{d_i}^{(\lambda, -d_i)} &= G_{d_i} - V^{(\lambda)}(i, :)t \\ &= G_{d_i} - s_{d_i}^{(\lambda)} - V^{(\lambda)}(i, i)(s_{d_i}^{(\lambda, -d_i)} - G_{d_i}) \end{aligned}$$

Solve for  $G_{d_i} - s_{d_i}^{(\lambda, -d_i)}$ ,

$$G_{d_i} - s_{d_i}^{(\lambda, -d_i)} = \frac{G_{d_i} - s_{d_i}^{(\lambda)}}{1 - V^{(\lambda)}(i, i)}. \quad (2.24)$$

So the *GCV* in (2.23) is rewritten using (2.24)

$$GCV(s, \lambda) = \frac{1}{M} \sum_{i=1}^M \left( \frac{G_{d_i} - s_{d_i}^{(\lambda)}}{1 - M^{-1} \text{trace}(V^{(\lambda)})} \right)^2, \quad (2.25)$$

which reduces the computation from  $M + 1$  splines down to 1! For a fixed  $\lambda$ , the weights for  $s^{(\lambda)}$  can then be computed from (2.16).  $\lambda$  is chosen as the minimizer of Equation 2.25.

The formulation in (2.25) hinges on the existence of  $V^{(\lambda)}$  which satisfies the relationship in (2.22). Now we will develop an expression for such a  $V^{(\lambda)}$  (Green and Silverman (1994, §8.2.1)). Recall  $s_{d_i}^{(\lambda)} = Z(i, :)\alpha + D^T(i, :)\beta$  from Proposition 1. Use  $Q_1, Q_2$  from QR-decomposition of (2.20) to expand  $Z\alpha$

$$Z\alpha = Q_1Q_1^T Z\alpha + Q_2Q_2^T Z\alpha$$

and Equation (2.17) to substitute for the second  $\alpha$

$$Z\alpha = Q_1Q_1^T Z\alpha + Q_2(Q_2^T ZQ_2\nu).$$

Combine (2.19) (which gives a substitution for  $Q_2^T ZQ_2$ ) and  $\nu$  from (2.21) to obtain

$$Z\alpha = Q_1Q_1^T Z\alpha + Q_2(I - \lambda U(\Sigma^2 + \lambda MI_{(M-3)\times(M-3)})^{-1}U^T)Q_2^T g.$$

Several steps of algebra later, one can show that

$$Z\alpha = Q_1Q_1^T Z\alpha + Q_2U\Sigma^2(\Sigma^2 + \lambda MI)^{-1}U^T Q_2^T g \quad (2.26)$$

Next, we expand  $D\beta$  with its QR-decomposition and substitute (2.18) for  $\beta$ ,

$$D\beta = Q_1R_1R_1^{-1} (Q_1^T g - Q_1^T ZQ_2\nu).$$

Replace  $Q_2\nu$  with  $\alpha$ ,

$$D\beta = Q_1Q_1^T g - Q_1Q_1^T Z\alpha. \quad (2.27)$$



Upon combining the expressions in (2.26) and (2.27), the  $Q_1 Q_1^T Z \alpha$  cancels, and we are left with

$$Z \alpha + D \beta = (Q_2 U \Sigma^2 (\Sigma^2 + \lambda M I)^{-1} U^T Q_2^T + Q_1 Q_1^T) g,$$

showing

$$V^{(\lambda)} = (Q_2 U \Sigma^2 (\Sigma^2 + \lambda M I)^{-1} U^T Q_2^T + Q_1 Q_1^T). \quad (2.28)$$

This explicit formulation allows for the determination of equivalent expressions for  $\text{trace}(V^{(\lambda)})$  and  $\sum_{i=1}^M (G_{d_i} - s_{d_i}^{(\lambda)})^2$ , both of which are necessary for *GCV* in (2.25) (Green and Silverman (1994, §8.2.1)).

We take the trace of the expanded version of  $V^{(\lambda)}$

$$\text{trace}(V^{(\lambda)}) = \text{trace} \left( \begin{pmatrix} Q_1 & Q_2 U \end{pmatrix} \begin{pmatrix} I_{3 \times 3} & 0_{3 \times (M-3)} \\ 0_{(M-3) \times 3} & \Sigma^2 (\Sigma^2 + \lambda M I)^{-1} \end{pmatrix} \begin{pmatrix} Q_1^T \\ U^T Q_2^T \end{pmatrix} \right).$$

The orthogonality of the  $Q$ 's together with the property that  $\text{trace}(AB) = \text{trace}(BA)$  for any matrices  $A$  and  $B$  reduces the trace to

$$\begin{aligned} \text{trace}(V^{(\lambda)}) &= \text{trace} \begin{pmatrix} I_{3 \times 3} & 0_{3 \times (M-3)} \\ 0_{(M-3) \times 3} & \Sigma^2 (\Sigma^2 + \lambda M I)^{-1} \end{pmatrix} \\ &= 3 + \sum_{i=1}^{M-3} \frac{\Sigma(i, i)^2}{\Sigma(i, i)^2 + \lambda M}. \end{aligned}$$

After adding and subtracting  $\lambda M$  in the numerator, the trace reduces to

$$\text{trace}(V^{(\lambda)}) = \sum_{i=1}^{M-3} -\frac{\lambda M}{\Sigma(i, i)^2 + \lambda M} + M. \quad (2.29)$$

Finally, we examine  $\sum_{i=1}^M (G_{d_i} - s_{d_i}^{(\lambda)})^2$ , which in matrix-vector form is  $\|(I_{M \times M} - V^{(\lambda)})g\|^2$ .

For the matrix difference inside the norm, it is convenient to again use the expanded form of  $V^{(\lambda)}$ ,

$$\begin{aligned} I_{M \times M} - V^{(\lambda)} &= Q \begin{pmatrix} I & 0 \\ 0 & U \end{pmatrix} \left( I - \begin{pmatrix} I_{3 \times 3} & 0_{3 \times (M-3)} \\ 0_{(M-3) \times 3} & \Sigma^2(\Sigma^2 + \lambda IM)^{-1} \end{pmatrix} \right) \begin{pmatrix} I & 0 \\ 0 & U \end{pmatrix}^T Q^T \\ &= Q \begin{pmatrix} I & 0 \\ 0 & U \end{pmatrix} \begin{pmatrix} 0_{3 \times 3} & 0_{3 \times (M-3)} \\ 0_{(M-3) \times 3} & I_{(M-3) \times (M-3)} - \Sigma^2(\Sigma^2 + \lambda IM)^{-1} \end{pmatrix} \begin{pmatrix} I & 0 \\ 0 & U \end{pmatrix}^T Q^T \\ &= Q \begin{pmatrix} I & 0 \\ 0 & U \end{pmatrix} \begin{pmatrix} 0_{3 \times 3} & 0_{3 \times (M-3)} \\ 0_{(M-3) \times 3} & \lambda(\Sigma^2 + \lambda IM)^{-1} \end{pmatrix} \begin{pmatrix} I & 0 \\ 0 & U \end{pmatrix}^T Q^T, \text{ where} \end{aligned}$$

the omitted dimensions of  $\begin{pmatrix} I & 0 \\ 0 & U \end{pmatrix}$  are

$$\begin{pmatrix} I_{3 \times 3} & 0_{3 \times (M-3)} \\ 0_{(M-3) \times 3} & U \end{pmatrix}.$$

Consolidate into the 2-norm,

$$\begin{aligned} \|(I - V^{(\lambda)})g\|^2 &= g^T \begin{pmatrix} Q_1 & Q_2 \end{pmatrix} \begin{pmatrix} I & 0 \\ 0 & U \end{pmatrix} \begin{pmatrix} 0_{3 \times 3} & 0_{3 \times (M-3)} \\ 0_{(M-3) \times 3} & \lambda^2(\Sigma^2 + \lambda MI)^{-2} \end{pmatrix} \begin{pmatrix} I & 0 \\ 0 & U \end{pmatrix}^T \begin{pmatrix} Q_1^T \\ Q_2^T \end{pmatrix} g \\ &= g^T \begin{pmatrix} Q_1 & Q_2 U \end{pmatrix} \begin{pmatrix} 0_{3 \times 3} & 0_{3 \times (M-3)} \\ 0_{(M-3) \times 3} & \lambda^2(\Sigma^2 + \lambda MI)^{-2} \end{pmatrix} \begin{pmatrix} Q_1^T \\ U^T Q_2^T \end{pmatrix} g \\ &= \lambda^2 g^T Q_2 U (\Sigma^2 + \lambda MI)^{-2} U^T Q_2^T g. \end{aligned}$$

Now we are ready to substitute the expressions for  $\text{trace}(V^{(\lambda)})$  and  $\|(I_{M \times M} - V^{(\lambda)})g\|^2$

into the  $GCV$  in (2.25)

$$GCV(s, \lambda) = M \frac{g^T Q_2 U (\Sigma^2 + \lambda M I)^{-2} U^T Q_2^T g}{\left( \sum_{i=1}^{M-3} (\Sigma(i, i)^2 + \lambda M)^{-1} \right)^2} \quad (2.30)$$

The expression in (2.30) is minimized over  $\lambda > 0$  to obtain the  $\lambda$  parameter for the final smoothing model. Once the penalization parameter is selected, the  $\lambda$  notation is dropped from  $s$ .

### From smoothing splines to Event-Related Causality

In seeking to infer significant *event-related* changes, time windows were classified as baseline or post-stimulus. for ERC, baseline windows were 250ms long and non-overlapping, covering -700ms to -200ms prior to stimulus onset. Each window was indexed by its starting value,  $b$ ,  $b \in \{1, 2\}$ . Post-stimulus windows covered two different periods, each with a window length of 100ms and window shift 50ms. These windows have indices  $p$ ,  $p \in \{1, \dots, P\}$ , regardless of the post-stimulus period (differentiating between post-stimulus periods in the notation is irrelevant to the current discussion of ERC).

ERC tests whether post-stimulus smoothed trends differ significantly from baseline values by constructing joint 95% confidence around the difference of baseline and post-stimulus  $s$  values at a fixed frequency. The uncorrected 95% confidence of the smoothed SdDTF value at an arbitrary time/frequency point  $d_i = (\tau_k, f_w)$  is (Wahba (1983); Wendelberger (1981); Wang and Wahba (1994))

$$s_{k,w} \pm 1.96(\sigma^2 V^{(\lambda)}(i, i))^{1/2},$$

where the error variance ( $\sigma^2$  from (2.12)) is estimated from (Green and Silverman (1994);

Wendelberger (1981))

$$\sigma^2 = \frac{\|g - V^{(\lambda)}g\|^2}{\text{trace}(I_{M \times M} - V^{(\lambda)})}.$$

Let  $e_{d_i} = (\sigma^2 V^{(\lambda)}(i, i))^{1/2}$ . Then the joint 95% confidence interval for post-stimulus window  $p$  and baseline window  $b$  is (Wang and Wahba (1994))

$$s_{b,w} - s_{p,w} \pm z_{.025} \sqrt{e_{b,w}^2 + e_{p,w}^2}, \text{ where} \quad (2.31)$$

$z_{.025}$  is the Bonferonni corrected  $z$ -score for 95% significance level. Under no correction, the  $z$ -score of 1.96 corresponds to the significance level of  $1 - .05$  (for a two-sided standard normal distribution). To correct for multiple comparisons,  $z_{.025}$  is the  $z$ -score which corresponds to the  $1 - .05/(n_e(n_e - 1)BP)$  confidence level.

The interval in (2.31) was computed for  $b = 1, \dots, B$  to determine the event-related significance in post-stimulus window  $p$ . If 0 is not contained in any of these intervals, we can presume with 95% confidence that  $s_{p,w}$  significantly differs from *all* baseline values. In contrast to Korzeniewska et al. (2008, 2011) we retained all significant  $s$  values, whether they were an average increase or decrease from baseline. We accounted for areas of negative change over baseline by excluding regions which showed deactivation after stimulus onset (negative percent change in the SB-MEMA results in Figure 3.1).

The ERC procedure for one patient terminates after all electrode pairs in  $J_{n_e}$  have been tested. A simplified diagram of ERC is in Figure 2.4. The chart assumes that the electrode pair  $(m, n)$  is fixed and excludes the check for  $p \leq P$  and  $w \leq n_f$ . The  $s$  values for the  $(m, n)$  pair of electrodes are represented as the grid in the top left. The procedure begins by initializing baseline and post-stimulus windows. Significance of each post-stimulus window

at frequency  $f_w$  is tested. We focus on one frequency within the diagram, and during the actual ERC procedure, all frequencies are tested.

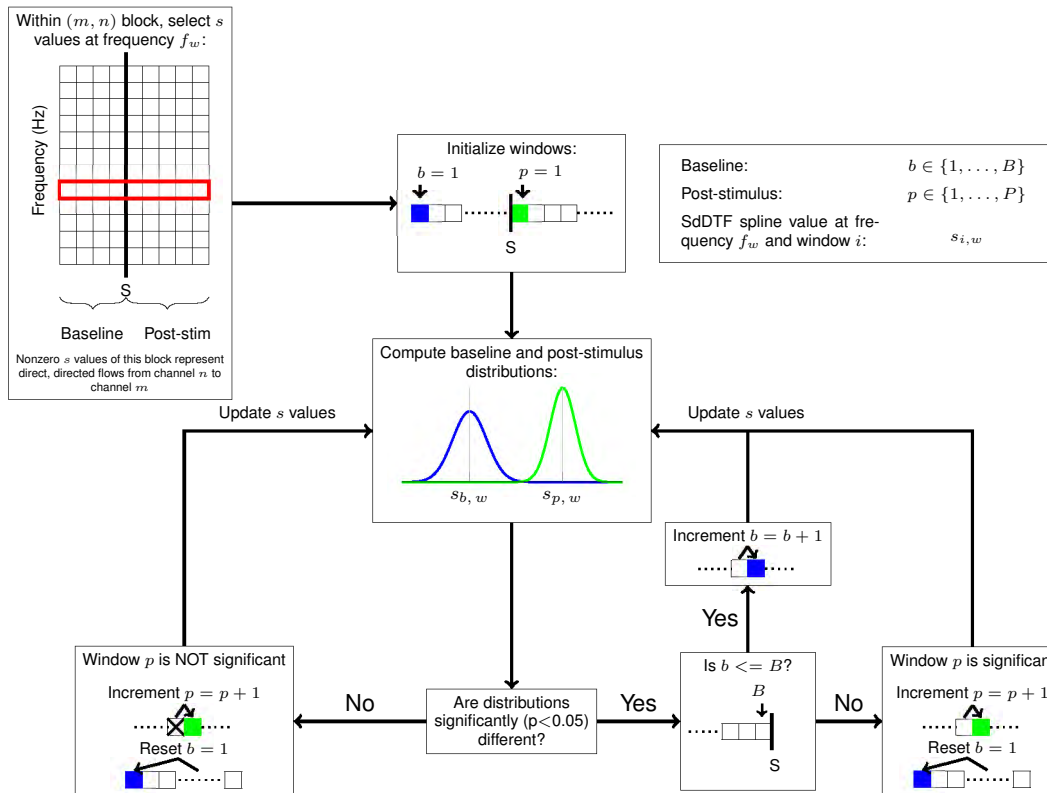


Figure 2.4 : Diagram of the ERC testing framework showing the sequence of steps that were followed for a fixed  $f_w$  and electrode pair  $(m, n)$ . Every baseline/post-stimulus pair of windows is tested for significance. This diagram excludes the check for  $p \leq P$  and  $w \leq n_f$  for simplicity.

As with SB-MEMA, trials were aligned to stimulus onset and RT. For stimulus (RT) aligned trials, post-stimulus SdDTF values were calculated over 100ms windows with a 50ms shift starting values from 50-650ms (RT-750ms to RT-100ms). Baseline SdDTF values were computed over two non-overlapping 250ms windows from -700ms to -200ms. The significant post-stimulus flows identified with the ERC method as  $\tilde{s}$ , where

$$\tilde{s}_{i,w}(m,n) = \begin{cases} s_{i,w}(m,n) & \text{if } s_{i,w}(m,n) \text{ is significant} \\ 0 & \text{otherwise} \end{cases}$$

for  $1 \leq i \leq P$ ,  $1 \leq w \leq n_f$ , and  $1 \leq m, n \leq n_e$ .

All signals were included for the SdDTF computations, and with the goal of describing interactions between distinct anatomical regions, flows sent and received by the same region were excluded. We acknowledge that intraregional communication is relevant to understand how reading processes are performed. Furthermore, grouping electrodes by anatomical location risks losing spatial information. However as a step toward elucidating regional effective connectivity, we believe, as others have similarly done (Flinker et al. (2015)), that focusing on interregional flows does not diminish the language network dynamics derived and offers valuable information about the regional dynamics.

The *interregional* ERC (post-stimulus) flows were integrated over 60-120Hz to compress each flow to a time-dependent scalar value. If the integrated ERC flow during time window  $i$  is referred to as  $\tilde{s}_i$ , then the integration over frequencies from electrode  $k$  to electrode  $j$  is calculated from

$$\tilde{s}_i(j,k) = \Delta w \sum_{w=1}^{n_f} \tilde{s}_{i,w}(j,k). \quad (2.32)$$

Finally, the frequency integrated ERC flows were averaged by region. To be clear, assume during time window indexed by  $i$  that  $r_n$  is the set of electrodes in region  $n$  (our analysis was performed over six anatomical regions, which will be given in Chapter 3) and let  $\tilde{s}_i^z(j, k)$  denote the flows from patient  $z$  between these regions. Then the average flow from region  $m$  to region  $n$  across all patients was computed using

$$\frac{\sum_{z=1}^{15} \sum_{j \in r_n} \sum_{k \in r_m} \tilde{s}_i^z(j, k)}{\text{length} \left( \sum_{z=1}^{15} \sum_{j \in r_n} \sum_{k \in r_m} \tilde{s}_i^z(j, k) \right)}.$$

### 2.8.2 Approach 2: statistical testing of post-stimulus, interregional SdDTF values

The ERC technique evaluates significance of post-stimulus smoothed SdDTF values at each time/frequency value. To gain a meaningful view of the network, the remaining significant smoothed SdDTF flows are integrated over frequencies and averaged by region. As the baseline flows have not been reduced by any statistical test, a comparison to the frequency integrated, regional averaged smoothed SdDTF values would be unfair at this point. Because the state of the network at baseline is the foundation for ERC, we decided to modify the statistical testing framework to allow for a more direct comparison between baseline and post-stimulus frequency integrated, regional averaged SdDTF values.

For the second approach of testing event-related changes in the network, SdDTF values were first computed on 100ms windows with a shift of 50ms over windows with starting values from 50-650ms period following stimulus onset (for stimulus aligned trials) and for starting values from RT-750ms to RT-100ms (for articulation aligned trials). Baseline SdDTF values

were computed on one 500ms pre-stimulus window from -700ms to -200ms. After integrating SdDTF values over frequencies,

$$G_i = \Delta w \sum_{w=1}^{n_f} G_{i,w},$$

where the time window indexed by  $i$  falls within baseline or either one of the post-stimulus periods, the average flow from region  $m$  to region  $n$  across all patients was determined via

$$\frac{\sum_{z=1}^{15} \sum_{j \in r_n} \sum_{k \in r_m} G_i^z(j, k)}{\text{length} \left( \sum_{z=1}^{15} \sum_{j \in r_n} \sum_{k \in r_m} G_i^z(j, k) \right)}. \quad (2.33)$$

$r_n$  is the set of electrodes situated in region  $n$  and  $G_i^z(j, k)$  denotes flows from electrode  $k$  to electrode  $j$  during the time window indexed by  $i$  for patient  $z$ . A Wilcoxon signed rank test was performed on the percent change of average interregional post-stimulus values versus baseline (2.33) at a  $p=0.001$  level (corrected for multiple comparisons with false discovery rate, FDR).

## 2.9 Table of abbreviations for Chapter 2

We conclude Chapter 2 with a table of abbreviations.



RT	reaction time
$N_s$	total number of samples per trial
$n_\tau$	number of 100ms windows
$n_s$	number of data samples with each 100 ms window
$n_t$	number of total trials
$n_e$	number of electrodes used in the analysis for patient $i$
$n_f$	number of frequencies
$\Delta t$	length of time between samples
$w$	frequency index
$f_w$	frequency
$p$	post-stimulus time window index
$b$	baseline time window index
$G_{i,w}(m, n)$	SdDTF value from electrode $m$ to electrode $n$ at frequency $f_w$ during time window $\tau_i$
$s_{i,w}(m, n)$	smoothed SdDTF value from electrode $m$ to electrode $n$ at frequency $f_w$ during time window $\tau_i$
$\tilde{s}_{i,w}(m, n)$	significant post-stimulus smoothed SdDTF value from electrode $m$ to electrode $n$ at frequency $f_w$ during time window $\tau_i$
SE	standard error
FDR	false discovery rate

Table 2.3 : Table of abbreviations.

## Chapter 3

### Results

#### 3.1 SB-MEMA ECoG maps

Results from the SB-MEMA are represented on the standard N27 surface in Figure 3.1. In the 50-750ms following stimulus onset (left), positive activations are seen in the fusiform gyrus and a ventral region at the junction of pre and postcentral gyri. As previously mentioned, positive activations near the fusiform gyrus during early pre-lexical processing are a trademark of reading tasks (Nobre et al. (1994); Dehaene and Cohen (2011); Price and Devlin (2003)). Interestingly, regions in lateral parietal cortex and the middle temporal gyrus deactivate from baseline during this period, which contrasts with fMRI (Jobard et al. (2003); Levy et al. (2008); Joseph et al. (2001)) and ECoG (Mainy et al. (2008)) word reading analyses. Also seen are drops from baseline across extensive orbitofrontal and temporal polar cortex.

During the 750ms prior to articulation onset (right), activity spreads anteriorly to regions including pars triangularis and pars opercularis of Broca's area, as well as pre, post, and subcentral gyri. The absence of activity across the middle and superior temporal lobes differs from many fMRI reading analyses which typically observe activations in these areas during semantic tasks (Fiez and Petersen (1998); Price (2012)).

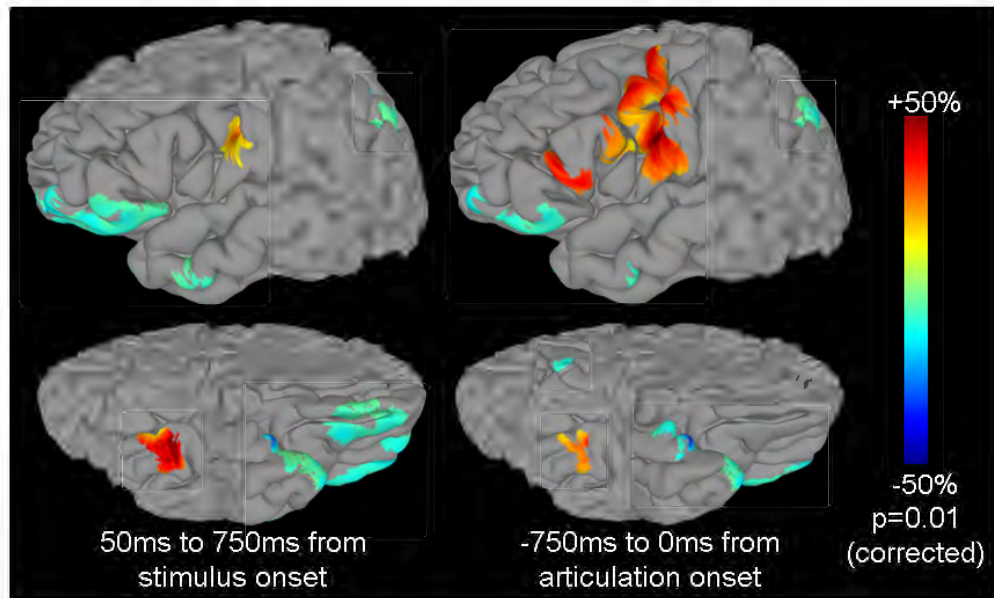


Figure 3.1 : Lateral (above) and ventral (below) views of the SB-MEMA maps of post-stimulus percent change from baseline for (left) trials aligned to stimulus onset (0ms) from 50-750ms and (right) RT-aligned trials during the 750ms leading up to RT. The heat map shows significant ( $p=0.01$ , corrected), percent changes from baseline, which is -700ms to -200ms prior to stimulus onset.

Despite some differences, the maps of regional activations shown in Figure 3.1 are largely consistent with those produced from years of neuroimaging and ECoG experiments during word reading tasks. Motivated by prior work (Korzeniewska et al. (2008, 2011)) which focused on regions with positive SdDTF changes from baseline, we continued the investigation by focusing on quantifying the interactions of regions with *positive* percent changes in Figure 3.1. Those regions which showed interesting deactivations in Figure 3.1 will be revisited in the discussion.

### 3.2 Regional mid-gamma time series

Electrodes situated over locations of positive percent change during either time period of Figure 3.1 were identified and classified by anatomical location, resulting in six total regions: fusiform, precentral, postcentral, subcentral, pars opercularis, and pars triangularis. As the SB-MEMA results provide summaries over periods exceeding 700ms, time traces of regional averaged mid gamma percent change in power from baseline (-700ms to -200ms before stimulus) were produced to supply insight into the transient changes prior to characterizing interregional interactions with the SdDTF. To compute these time traces, the raw ECoG data from each electrode were bandpass filtered into the mid-gamma frequency range (IIR Elliptical Filter, 30dB sidelobe attenuation). The data were then Hilbert transformed, and the analytic amplitude was smoothed (Savitzky-Golay FIR, 5<sup>th</sup> order, frame length of 155 samples, Matlab 2013b, Mathworks, Natick MA). For all remaining figures, each region is assigned a color: fusiform is green, precentral is orange, postcentral is cyan, subcentral is purple, pars opercularis is blue, and pars triangularis is red (reference the Table in Figure 3.2).

The time traces of regional percent change in power ( $\pm 1$  SE in the shaded area) for all 183 electrodes identified from the SB-MEMA analysis are in Figure 3.2. The electrodes are represented as spheres on the standard N27 surface. The number of electrodes per region is in parenthesis. Traces for both periods are shown on the right. A Wilcoxon signed rank test was implemented to identified times where power was significantly different from 0 ( $p=0.05$ , corrected for multiple comparisons using false discovery rate, FDR). The bars at the bottom

of each plot show the times where power achieved significance.

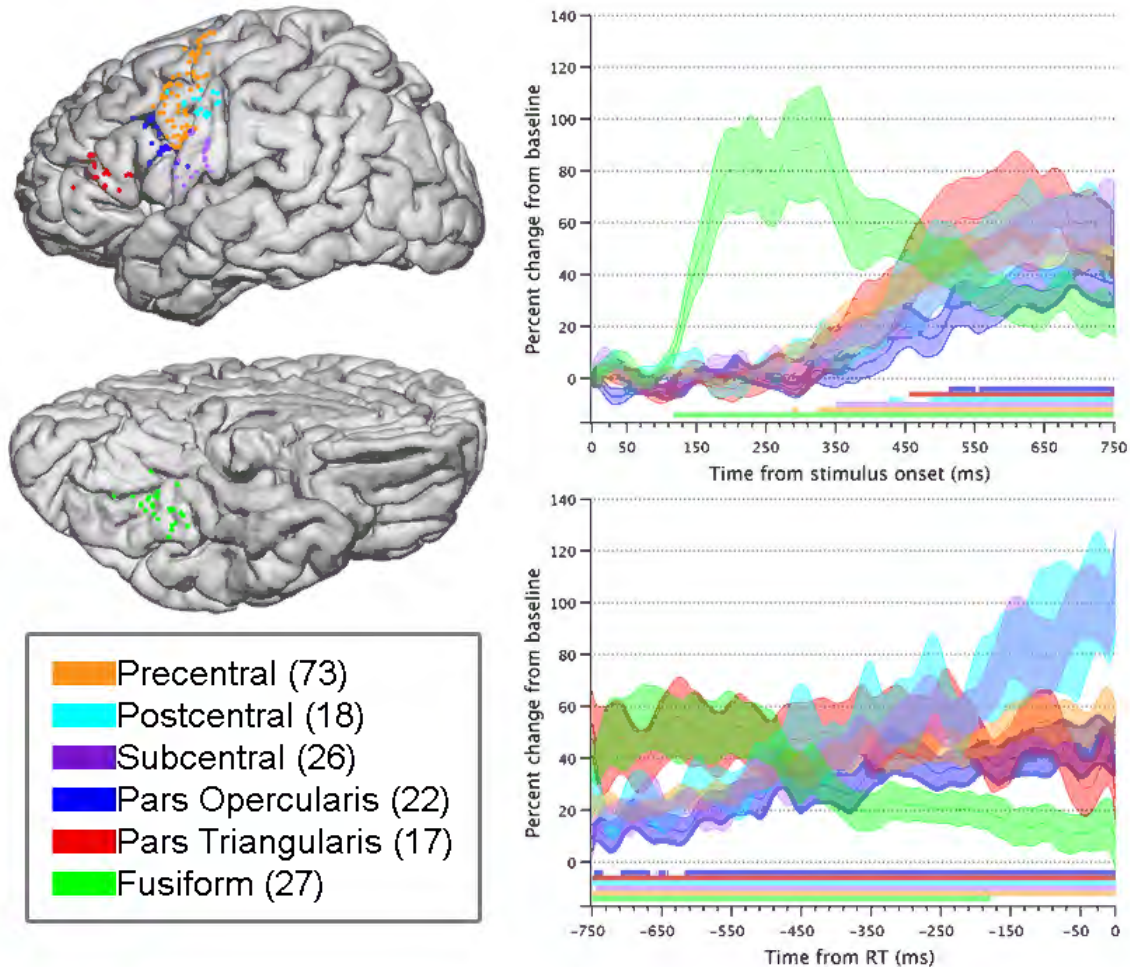


Figure 3.2 : (Left) 183 unique electrodes represented on the N27 surface were situated over the positively activated regions in either panel of Figure 3.1. The number in parenthesis indicates the number of electrodes included per region. (Right) Mean  $\pm 1$  SE of percent change in mid gamma power following stimulus onset (above) and leading up to RT (below). The bars at the bottom of each plot indicate times where percent change in power of each region is significantly different from 0 (Wilcoxon signed rank, FDR corrected,  $p=0.05$ ).

Recall that no articulation occurs during the period following stimulus onset (right, above), as trials with RT's less than 750ms were excluded from the analysis. Immediately following stimulus onset, fusiform signals show the earliest change in power, sharply increas-

ing from baseline around 100ms and peaking at about 120% by 300ms. The remaining areas gradually begin to increase beginning around the time of the fusiform decrease ( $\approx 300$  ms), with pars triangularis peaking around 80% by 600ms.

For trials locked to RT (right, below), pars triangularis and fusiform begin at levels above ( $\approx 50\%$ ) the remaining regions ( $\approx 20\%$ ). Sub and postcentral areas show the greatest increase as the period progresses, peaking around 100% by the onset of articulation (0ms). Fusiform gradually decreases in power during the several hundred milliseconds leading up to RT so that by RT, it is merely 15% above baseline levels. The traces from pars opercularis and precentral are around 20% at RT-750ms and increase to about 40% by RT (0ms). The average pars triangularis power remains steady around 50% from RT-750ms through RT-250ms, when it gradually decreases to about 30%.

The traces in Figure 3.2 provide *speculative* evidence that following stimulus onset and prior to RT, the fusiform is a driver of higher level functions performed (not necessarily exclusively by) locations within pars opercularis, pars opercularis, pre, post, and subcentral gyri, as their increasing power is immediately preceded by a decrease in the fusiform. It is less clear how all of the areas interact from the traces of Figure 3.2. About 350ms from RT, the fusiform power diverges from the others, while pars triangularis, precentral, and pars opecularis traces are similar, and postcentral and subcentral traces are also similar. To describe regional interactions with a quantified measure of information flow, including the direction and degree of interaction, all 183 unique electrodes pictured in Figure 3.2 were analyzed with the SdDTF.

### 3.3 Grouped effective connectivity network dynamics

The 183 electrodes identified through the SB-MEMA analysis are listed by region and patient in Table 3.1. Each patient’s set of electrodes, denoted in §2.6 as  $\{x^1, x^2, \dots, x^{n_e}\}$ , was analyzed with the SdDTF to characterize network dynamics during word stem completion.

Patient index	1	2	3	4	5	6	7	8	9	10	11	12	13	14	15	Total
Fusiform	4	6	2	3	0	1	1	2	0	0	0	2	1	2	3	27
Pars Opercularis	1	3	1	2	1	0	2	2	2	1	2	0	1	2	2	22
Pars Triangularis	0	1	2	3	1	2	0	1	1	0	2	0	2	2	0	17
Postcentral	0	1	0	0	2	2	1	1	2	2	1	2	2	1	1	18
Precentral	4	4	5	2	4	7	5	6	2	5	7	5	7	5	5	73
Subcentral	2	1	3	3	4	1	1	1	2	3	1	1	1	0	2	26
Total	11	16	13	13	12	13	10	13	9	11	13	10	14	12	13	183

Table 3.1 : Electrodes organized by patient and region that were analysis with the SdDTF to infer interregional information flow.

Frequency integrated interregional averaged values from ERC (discussed in §2.8) or strictly SdDTF (discussed in §2.8.2) will be referred to as ERC flows and SdDTF flows, respectively. In the case of ERC, significance testing occurred prior to integrating the SdDTF values, and in the case of the SdDTF flows, significance testing occurred after integration and regional averaging. The flows are shown ( $\pm 1$  standard error, or SE) in each figure to follow. The color of each marker denotes the region receiving the flow. Each point along a single time course corresponds to the magnitude of the same flow occurring during different windows. The horizontal axis labels reference the first point of each 100ms time window (e.g, the flow at 50ms was computed over the 50-150 ms window).

### 3.3.1 Flows from fusiform

#### Relative to stimulus onset

The regional power traces in Figure 3.2 indicate that fusiform peaks in power around 300ms after stimulus onset. The interactions determined through ERC stemming from fusiform to all other regions relative to stimulus onset are shown in the left columns of Figure 3.3. Feedforward flows to postcentral (3.3c) sharply increase just prior to 300ms, but their high variability makes the change difficult to interpret. All flows from fusiform in Figure 3.3 are lower around 300ms (compared to the 50ms window), suggesting a decrease in the feedforward interactions at this time. Flows to all regions increase in the final window, with those to subcentral (3.3e) and pars opercularis (3.3a) reaching their highest average for this timeframe.

The SdDTF flows in the left columns Figure 3.4 allow us to visualize the flows and their baseline values simultaneously. None of the flows to pars triangularis (3.4b) and postcentral gyrus (3.4c) reached significance from baseline, whereas nearly all those to pars opercularis did (3.4a). Several flows to subcentral (3.4c) and many flows to precentral (3.4d) were also identified as significantly different from baseline.

**Relative to articulation onset:** Figure 3.2 shows that fusiform power is decreasing toward baseline levels as articulation onset approaches. In the right columns of Figure 3.3, we see that the ERC flows from fusiform to all regions decrease following the first window (at RT-750ms). Yet as time progresses, all flows gradually approach (or surpass) their maximum



values during the final window, which immediately precedes the onset of articulation.

The SdDTF flows in the right columns of Figure 3.4 to pars opercularis, subcentral, and precentral are the only ones to achieve significance during this timeframe. Those to pars opercularis shift back and forth toward baseline. Those to subcentral primarily increase during the time frame leading up to RT.

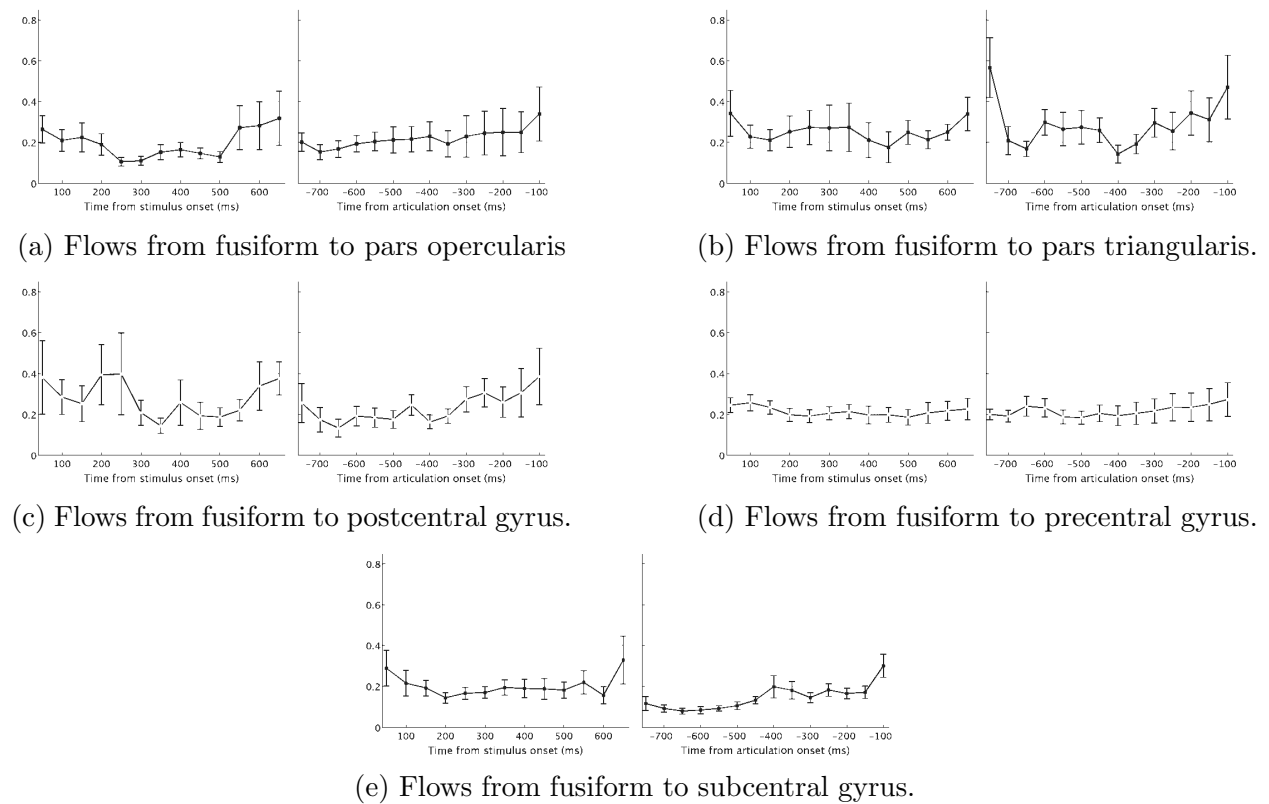


Figure 3.3 : ERC flows originating in fusiform. The left column is relative to stimulus onset, and the right column is relative to articulation onset.

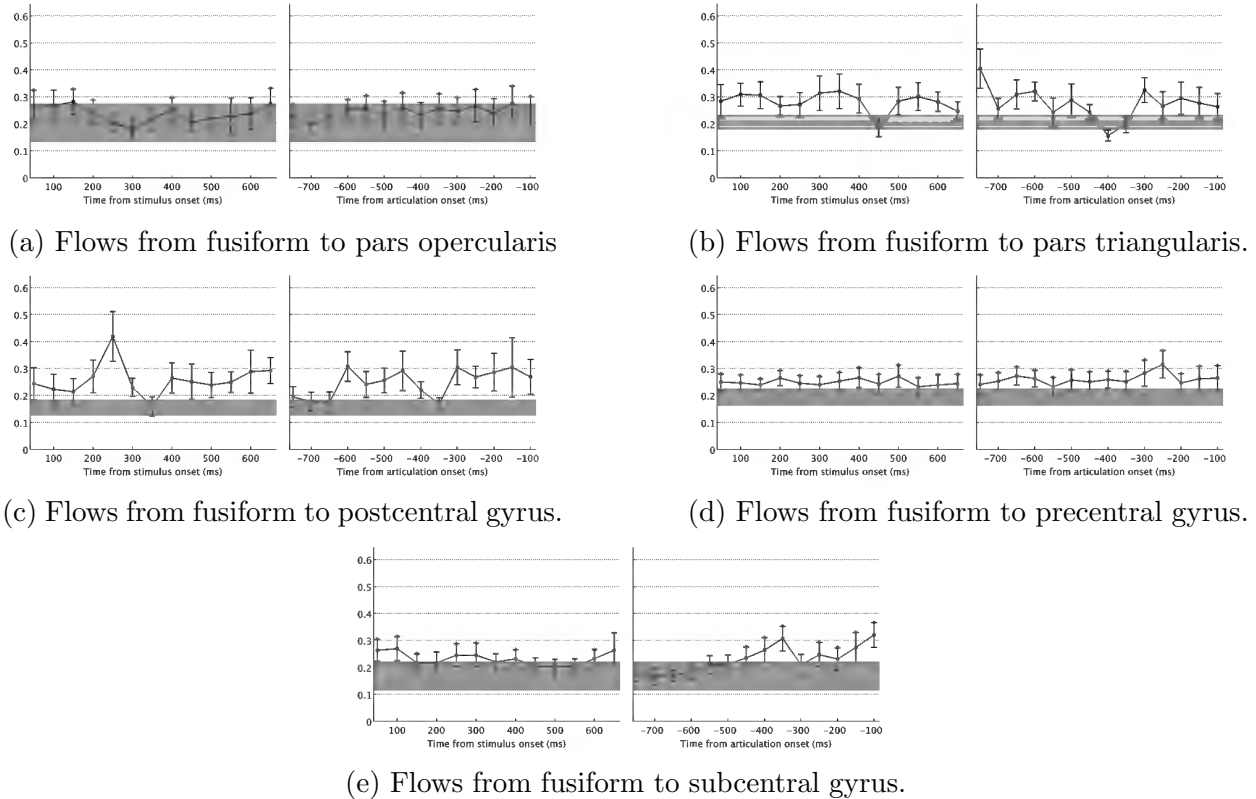


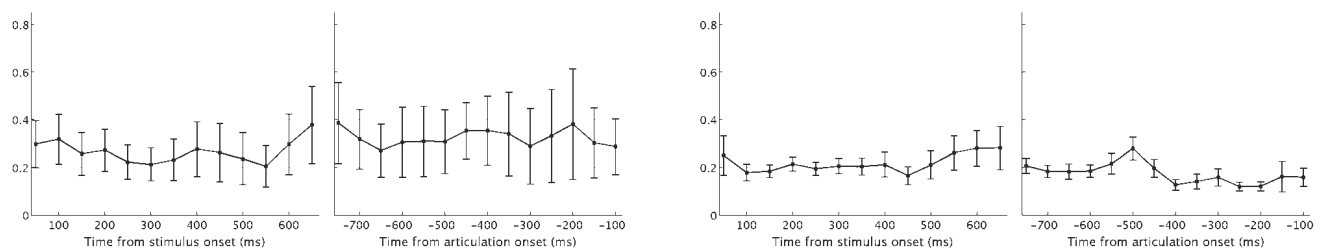
Figure 3.4 : SdDTF flows originating in fusiform. The left column is relative to stimulus onset, and the right column is relative to articulation onset. Red stars indicate time windows that reached significance versus baseline (Wilcoxon signed rank, FDR corrected for  $p=0.001$ ). Gray bars show baseline.

### 3.3.2 Flows from pars opercularis and pars triangularis

**Relative to stimulus onset:** Mid gamma power in both pars opercularis and pars triangularis regions begins to increase from baseline around 300ms (Figure 3.2). While pars triangularis decreases after it peaks around 600ms, pars opercularis continues to follow an upward trend. In Figures 3.5 and 3.6, we observe ERC and SdDTF flows originating from these regions. Similar to pars opercularis ERC interactions with fusiform, those from pars triangularis (in Figure 3.5b) increase (with their averages and standard error) during the

several hundred milliseconds leading up to the final window. SdDTF flows from pars triangularis (3.6b), on the other hand, increase earlier around 300ms, which more closely matches the timing of the mid-gamma increase of fusiform (in 3.2).

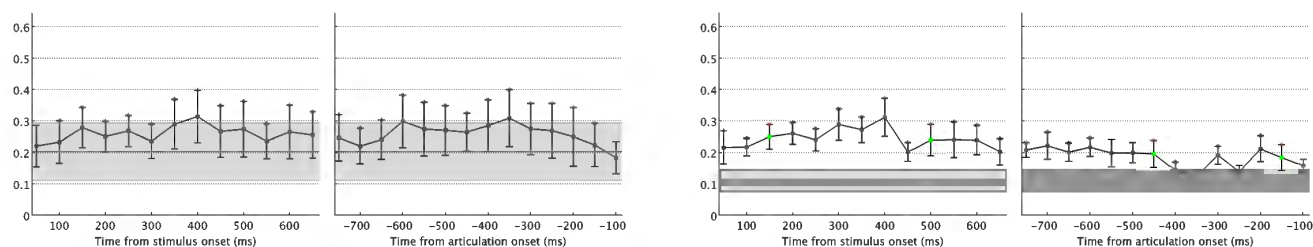
**Relative to articulation onset:** As power in pars opercularis gradually increases toward the onset of articulation (0ms in Figure 3.2), pars triangularis shifts in the opposite direction toward baseline. Average ERC and SdDTF flows to fusiform from pars opercularis (right columns of Figure 3.5a and 3.6a) are highly variable during the period leading up to articulation onset. Figure 3.5b shows that the ERC flows to pars triangularis reach a maximum around 500ms prior to articulation onset. Overall, Figure and 3.6b the SdDTF flows to pars triangularis remain above baseline around the same timeframe. Both ERC and SdDTF flows from pars triangularis decrease around RT-550ms and dance around increases and decreases leading up to RT.



(a) Flows from pars opercularis to fusiform.

(b) Flows from pars triangularis to fusiform.

Figure 3.5 : ERC flows to fusiform from regions in the inferior frontal gyrus. The left column is relative to stimulus onset, and the right column is relative to articulation onset.



(a) Flows from pars opercularis to fusiform.

(b) Flows from pars triangularis to fusiform.

Figure 3.6 : SdDTF flows to fusiform from regions in the inferior frontal gyrus. The left column is relative to stimulus onset, and the right column is relative to articulation onset. Red stars indicate time windows that reached significance versus baseline (Wilcoxon signed rank, FDR corrected for  $p=0.001$ ). The gray bar shows baseline.

### 3.3.3 Flows from precentral, postcentral, and subcentral gyri

**Relative to stimulus onset:** Similar to pars triangularis and pars opercularis, the grouped traces in Figure 3.2 illustrate that precentral, postcentral, and subcentral regions begin their increases in mid gamma power around 300ms. Both methods converge in showing flows from subcentral to fusiform (3.7c and 3.8c) increase to their maxima around 300ms. SdDTF flows from precentral to fusiform (3.8a) remain significantly above baseline, with only subtle changes (similar to the ERC flows). SdDTF interactions from postcentral in 3.8b show interesting dynamics around 300ms, similar to those from subcentral; however, none of the postcentral flows attain significance.

**Relative to articulation onset:** Precentral power follows a gradually increasing pattern during the windows leading up to articulation onset (Figure 3.2), while postcentral and subcentral gyri dramatically increase in power (up to 100% from baseline) by articulation onset. ERC and SdDTF flows from precentral relative to articulation onset (right columns of

Figures 3.7a and 3.8a) and subcentral (right columns of Figures 3.7c and 3.8c), are relatively steady. Those from postcentral are more dynamic, with several periods of brief increases and decreases (Figures 3.7c and 3.8c); although those from the non-ERC method are largely not significant and should not be considered different from baseline.

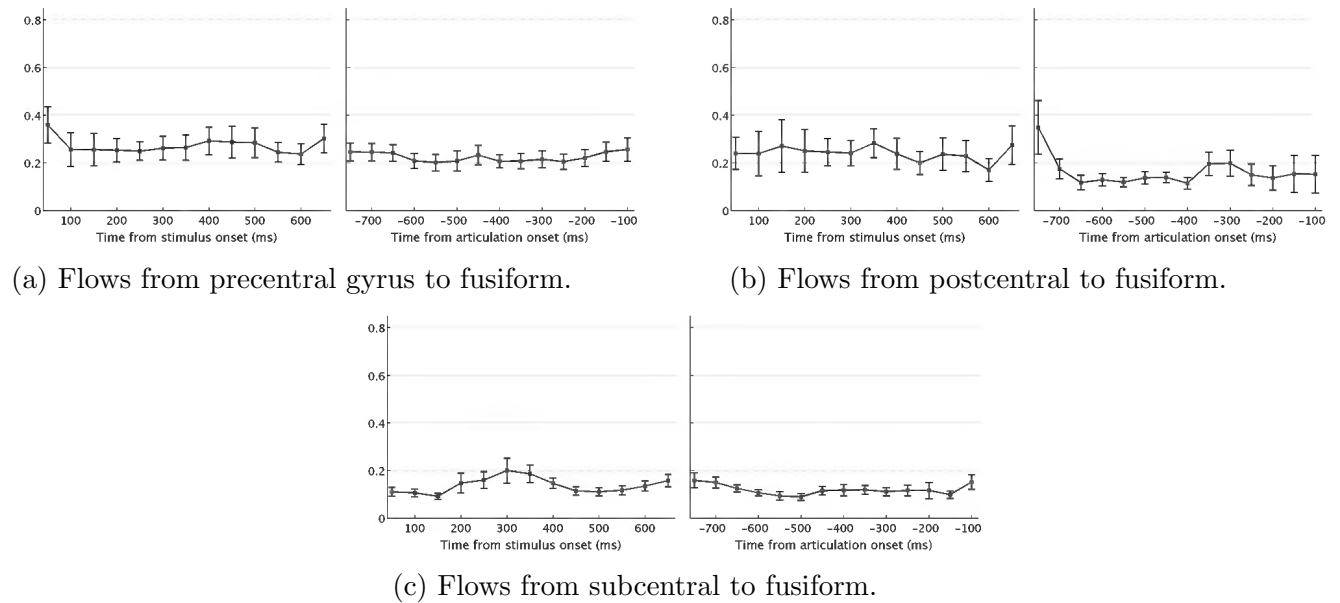


Figure 3.7 : ERC flows to fusiform from the three regions that border the central sulcus. The left column is relative to stimulus onset, and the right column is relative to articulation onset.

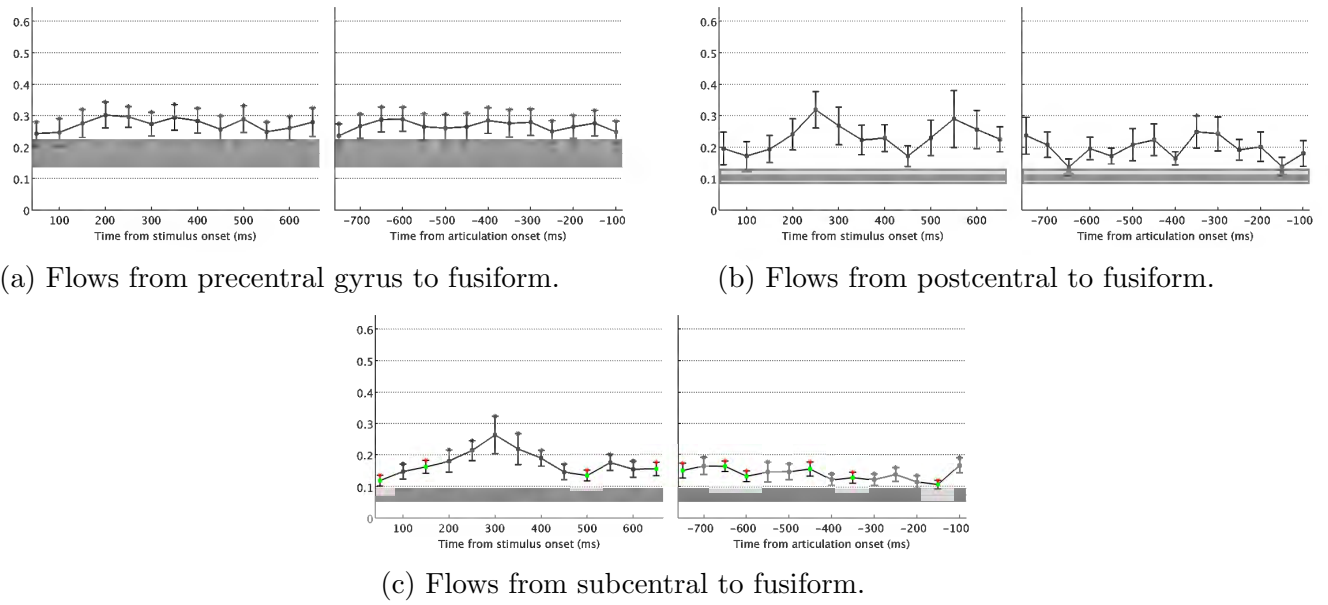


Figure 3.8 : SdDTF flows to fusiform from the three regions bordering the central sulcus. The left column is relative to stimulus onset, and the right column is relative to articulation onset. Red stars indicate time windows that reached significance versus baseline (Wilcoxon signed rank, FDR corrected for  $p=0.001$ ). The gray bar shows baseline.

## Chapter 4

### Discussion

Prior work (Price and Devlin (2011)) has hypothesized that fusiform integrates top-down (feedback) processes with bottom-up (feedforward) processes during the presentation of visual words to facilitate correct pronunciation. This framework, termed the Interactive Account, predicts that visual stimuli that are more familiar to the subject will rely more on feedback processes to achieve spoken response, while less familiar stimuli would rely more on feedforward processes. We sought to describe the spatiotemporal brain dynamics during a word completion task from 15 patients' ECoG time series using complementary techniques to precisely identify locations, timings, and directionality of information flow to test how our data agree with this model of word reading.

To narrow the scope of the processes engaged across the patient cohort, our analysis focused on the stimulus-aligned trials and articulation-aligned trials. The combined regions of interest identified with the SB-MEMA during both periods include: fusiform, pars triangularis, pars opercularis, precentral, postcentral, and subcentral (Figure 3.1). The precise times of transient, independent regional activity were approximated by computing the time course of average percent change in power of each region from baseline (Figure 3.2). An explanation of brain dynamics during word stem completion (with a focus on those involving fusiform gyrus) was developed using a precise measure of information flow, the SdDTF,

which characterizes whether information is being sent or received, and whether the flows are direct or indirect.

Post-stimulus flows were tested for significance against pre-stimulus baseline flows using two approaches. For Event-related Causality (ERC), SdDTF values were smoothed and tested for significance at every time window and frequency value. The values which survived the conservative significance test were integrated over frequencies and averaged by region. We adapted a modified framework, where all SdDTF values were integrated over frequencies, averaged by region, and then tested for significance (the resulting values were referred to as SdDTF flows). This approach enabled us to test the dynamics of the network at baseline. Our interpretations of the findings are now discussed.

#### **4.1 Interactions relative to stimulus onset**

The period when visual information enters higher level processing streams has enjoyed significant popularity in the word reading research due to activation of the vOT, located next to the fusiform. vOT has been proposed to be crucial to the function of the visual word form system (Dehaene et al. (2002)). Based on studies of word form dyslexic patients, the visual word form system was originally defined as “that which parses (multiply and in parallel) letter strings into ordered familiar units and categorizes these units visually” (Warrington and Shallice (1980)), forcing patients who suffer damage to this system to read in a slow, laborious letter-by-letter basis.

Subdural electrodes cannot record from directly from vOT, as it is located in the sulcus



separating occipital and temporal lobes (Dehaene et al. (2002)). During word stem, significant mid gamma activity was observed from a nearby cluster of 27 electrodes in fusiform (top right of Figure 3.2). Fusiform power peaked around 300ms after stimulus onset. By articulation (bottom right of Figure 3.2), these electrodes' mid gamma signals approached baseline levels.

Results from both statistical approaches revealed exchanges involving fusiform to regions associated with higher level processing. ERC flows from fusiform to all regions were lower around 300ms than during the first 50ms window and final 650ms window. In the reverse direction, the flows from subcentral, although increasing around the 300ms timeframe of the significant mid-gamma of fusiform, are small relative to all other flows of the network, which can be visualized in the interactions of the entire network in Figure 4.1. Pars opercularis, pars triangularis, and subcentral regions are involved with interactions of the greatest magnitude; however, ERC does not take variability of the flows into consideration at this point.

Traces of SdDTF flows appear to be more consistent with the timings of the mid-gamma power traces, with those from subcentral and pars triangularis to fusiform peaking around 300ms. Figure 4.2 shows the dynamics of the entire network during three post-stimulus windows, and highlights that fusiform and precentral are involved in many interactions of large magnitude. We can see the prominent feedback interactions from pars triangularis, as well as the central roles of precentral and fusiform to the the entire network, with clear increases to fusiform from pars triangularis in the 300ms window.

Both statistical approaches revealed bidirectional interactions involving fusiform through-

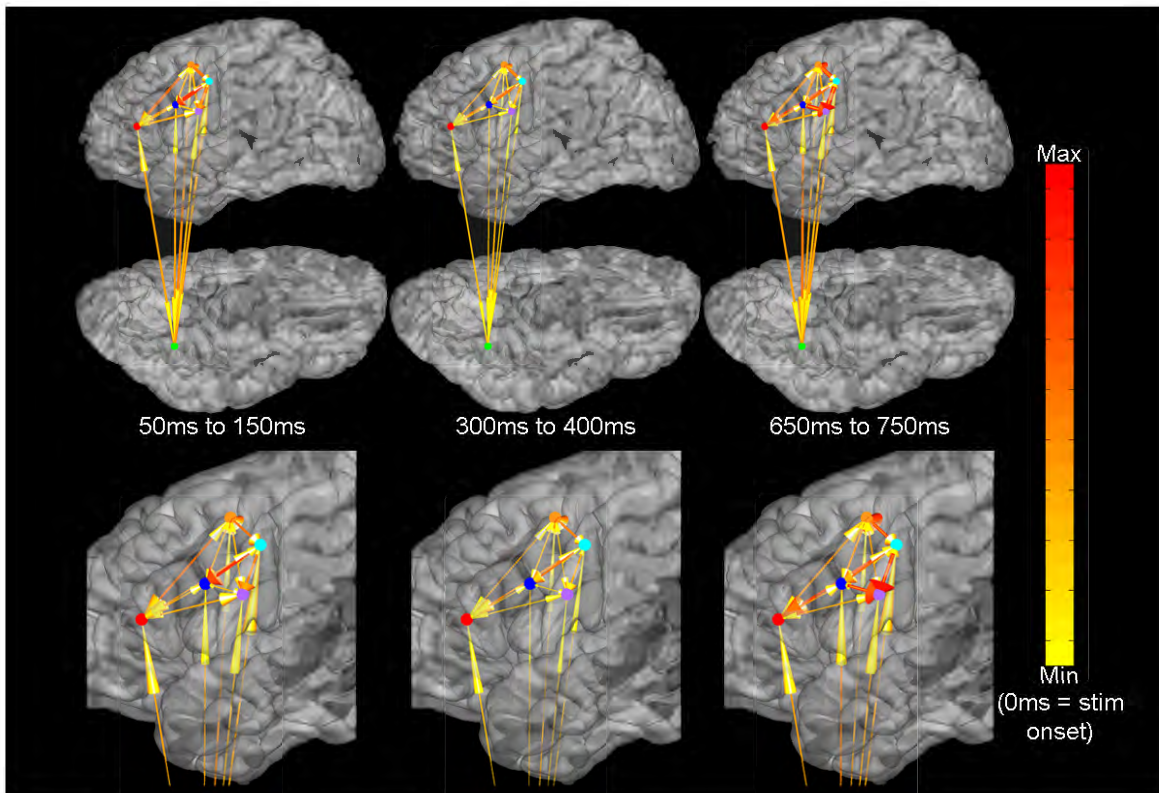


Figure 4.1 : ERC flows during three windows following stimulus onset. Top row shows lateral and ventral surfaces, and bottom row shows lateral surface enhanced. Regions are represented by a spheres. The color and width of each arrow is proportional to flow magnitude.

out the entire period following stimulus onset. ERC flows suggest that fusiform actively sends and receives information to all regions at various magnitudes, with many outgoing flows decreasing around 300ms. Around the same time, incoming flows from subcentral increase. Overall, interactions between fusiform and pars opercularis and pars triangularis were highly variable and difficult to interpret.

SdDTF flows from pars triangularis and subcentral to fusiform appeared to be more consistent with the patterns we observed in the fusiform mid gamma trace following stimulus onset. Pars triangularis and subcentral to fusiform flows peaked around 300ms (as did

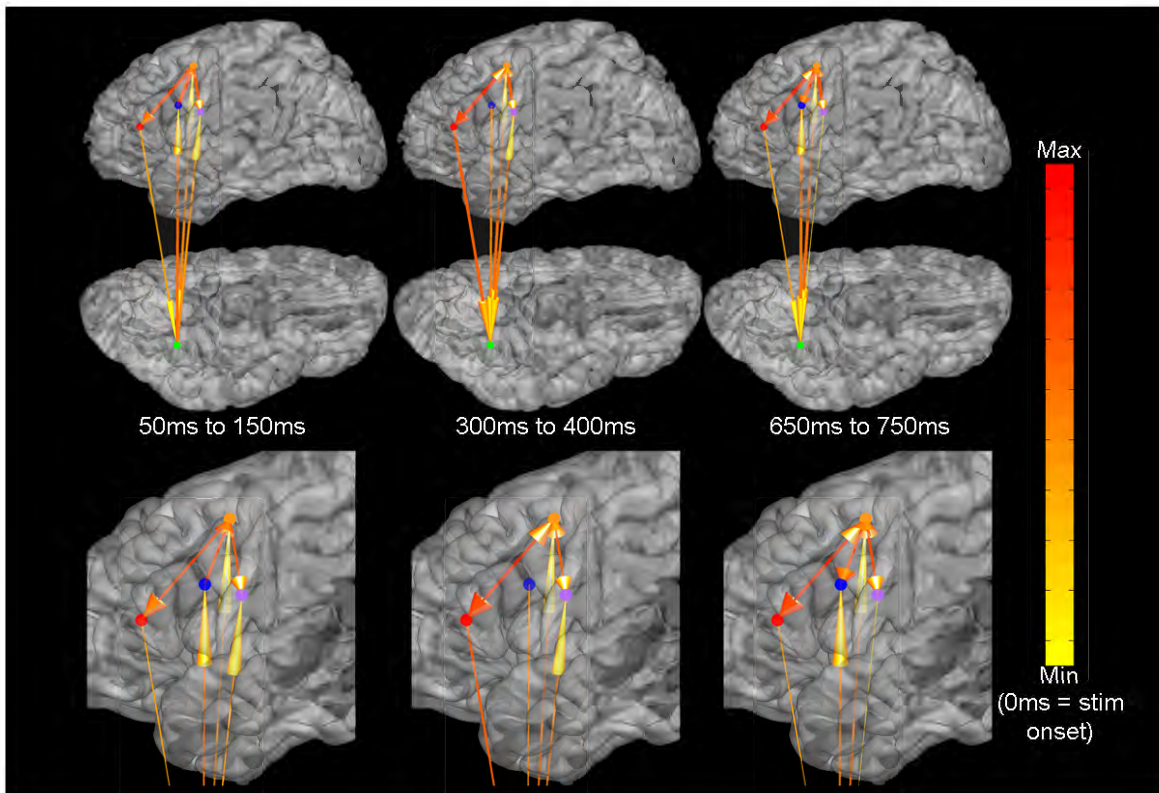


Figure 4.2 : Significant SdDTF flows during three windows following stimulus onset. Top row shows lateral and ventral surfaces, and bottom row shows lateral surface enhanced. Regions are represented by spheres. The color and width of each arrow is proportional to its flow.

postcentral to fusiform, although they did not achieve significance at the  $p=0.001$  level).

Overall, flows to and from precentral were above baseline levels.

## 4.2 Interactions relative to articulation onset

Following the peak of fusiform's mid gamma power, power begins to increase in the anterior locations of the network we identified as relevant to word stem completion, including pars triangularis and pars opercularis of the inferior frontal gyrus. These two neighboring regions

are generally associated with semantic and phonological processes, respectively (Bokde et al. (2001)); however, neither is purely dedicated to one function (Mainy et al. (2008); Jobard et al. (2003); Joseph et al. (2001); Sahin et al. (2009); Mechelli et al. (2005)). Because average pars triangularis power drops after 600ms, (right column of Figure 3.2), this region seems to be required less for phonological processing during word stem. Pars opercularis, on the other hand, shows positive changes from baseline after stimulus onset and prior to RT without reaching a peak of activity. Increased mid gamma response closer to articulation suggests that it is more dedicated to processes required immediately prior to articulation, such as those involving phonology or articulatory planning.

The ERC interactions in Figure 3.5 illustrate flows from both pars triangularis reach a peak around 500ms prior to RT, while those from pars opercularis are inconclusive (due to their high variability). In the reverse direction (3.3), ERC flows from fusiform to pars triangularis increase during the 400ms leading up to RT, while those to pars opercularis increase more gradually.

Figure 3.6 illustrates that significant SdDTF flows from both pars triangularis and pars opercularis to fusiform are present during the period relative to articulation onset; although neither of the traces include a clear increase, like the ERC flows from pars triangularis to fusiform flows did. In the reverse direction, only SdDTF flows from fusiform to pars opercularis achieved significance (3.4a).

Figures 4.3 and 4.4 show the network-level interactions deduced from both statistical approaches also include precentral, postcentral, and subcentral gyri. These three regions, which

border the central sulcus, are also known as the primary motor and ventral somatosensory cortices. Their positive shifts in mid gamma activity during word stem (Figure 3.1) prior to articulation agree with their involvement in phonological processing, as well as processing action words. Lesion patients who have presented with categorical lexical retrieval deficits (Damasio and Tranel (1993); Daniele et al. (1994)) have provided strong evidence for distinct pathways for accessing nouns and verbs. These studies indicate that nouns are retrieved by left ventral pathways, whereas verbs are accessed in left frontal regions (Damasio and Tranel (1993); Daniele et al. (1994); Hillis and Caramazza (1995)). This phenomenon of dissociated pathways (dorsal versus ventral) for word category (verb versus noun) has also been observed with ECoG (Conner et al. (2014)). In addition, the pre-articulatory responses of pre and postcentral gyri may suggest their roles in planning for feedback control during response (Bouchard et al. (2013)).

When fusiform is at its lowest point in mid-gamma power (near articulation onset, see 3.2), its ERC flows to postcentral (3.3c), precentral (3.3d), and subcentral (3.3e) reach their highest point. Flows to all three of these regions are overall increasing during the 400ms leading up to RT. ERC flows in the opposite direction (3.7) do not show readily distinguishably patterns.

SdDTF flows in Figure 3.8 and 3.3 indicate bidirection flows from precentral and subcentral to fusiform (and vice versa) are significant during this timeframe. Notably, interactions between fusiform to postcentral were not significant, although they were above baseline near RT.

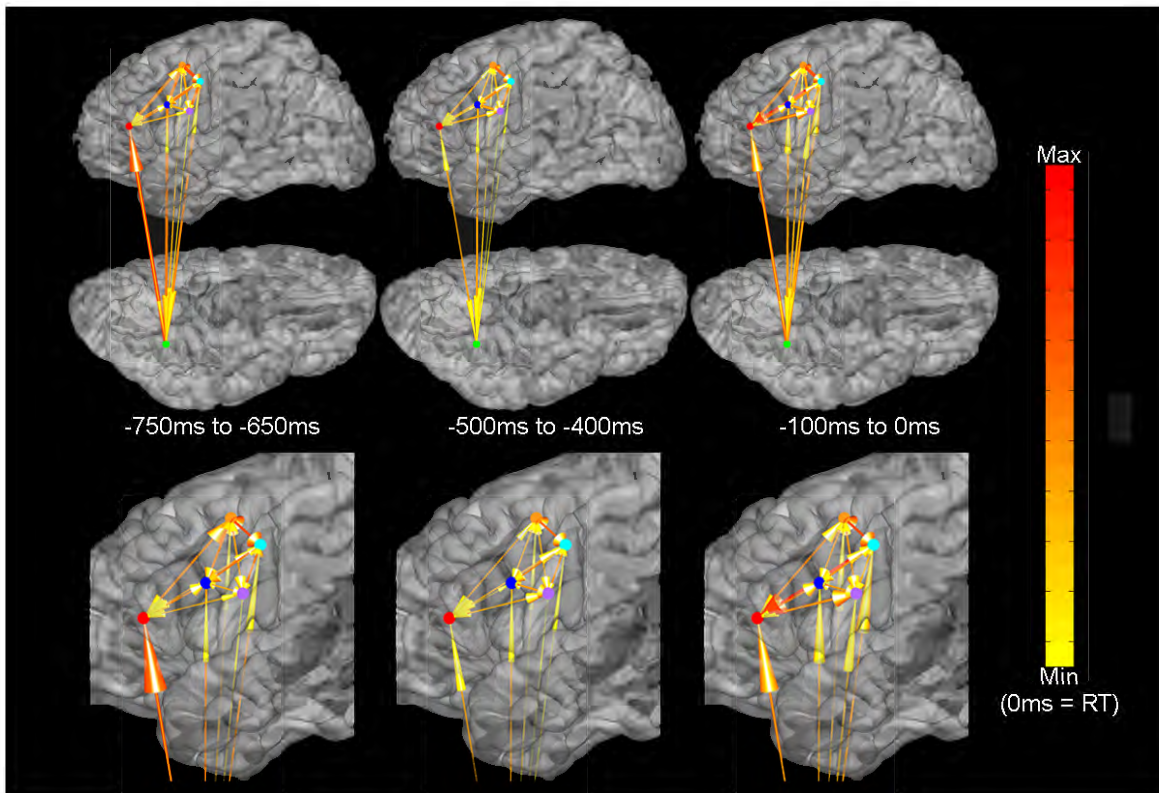


Figure 4.3 : ERC flows during three windows leading up to articulation onset. Top row shows lateral and ventral surfaces, and bottom row shows lateral surface enhanced. Regions are represented by a spheres. The color and width of each arrow is proportional to flow magnitude.

Taken together, the interactions relative to articulation onset suggest fusiform is deeply rooted in semantic, phonological, and articulatory planning processes during word stem completion. Regions sending information include pars triangularis (ERC and SdDTF flows), precentral (ERC and SdDTF flows), and subcentral (ERC and SdDTF flows). Pars opercularis flows to fusiform were highly variable with both analyses, although SdDTF flows from pars opercularis to fusiform were deemed significant. Important areas receiving information from fusiform include pars opercularis (ERC and SdDTF flows), pars triangularis (ERC



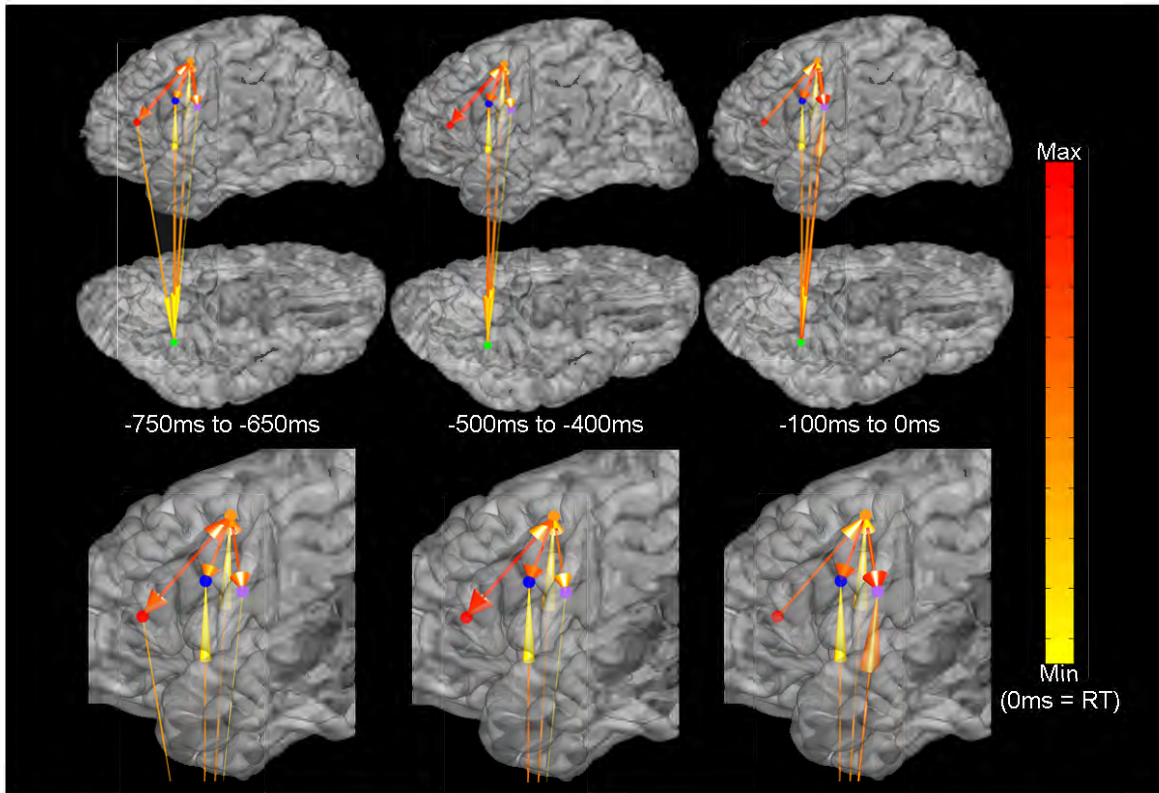


Figure 4.4 : Significant SdDTF flows during three windows leading up to articulation onset. Top row shows lateral and ventral surfaces, and bottom row shows lateral surface enhanced. Regions are represented by spheres. The color and width of each arrow is proportional to its flow.

flows), postcentral (ERC flows), precentral (ERC and SdDTF flows), and subcentral (ERC and SdDTF flows).

### 4.3 Limitations

Electrode coverage is a limitation that goes hand in hand with ECoG studies. Table 3.1 highlights that only three patients had coverage in all six regions. The remaining 12 patient-specific networks were incomplete due to limitations in the number of viable electrodes to

include. Our hope was that by averaging the flows across patients, the network dynamics that emerged would account for the patient-specific gaps. Coverage gaps can negatively impact the SdDTF analysis, which obviously cannot account for these excluded regions that may be required for the task.

Middle temporal, temporal polar, and lateral parietal cortices are frequently associated with semantic access (Joseph et al. (2001); Price (2012); Mainy et al. (2008); Dhond et al. (2001)), and were observed to deactivate following stimulus onset (Figure 3.1). Their deactivations could suggest that activity halted to facilitate the performance of regions more relevant to the task at hand, including pre, post, and subcentral gyri, (further analysis would be required to validate).

Six regions were ultimately identified through the SB-MEMA results and included in our analysis. The word reading network undoubtedly includes regions which extend beyond those reviewed in the current investigation. With a looser criteria for SB-MEMA ( $p=0.05$  instead of  $p=0.01$ , for instance), more locations would have been represented. The cost of including more regions is seen in the stringent correction in Equation 2.31), which makes it difficult to detect significance as the number of electrodes increases. Thus, there is a trade-off embedded within the ERC technique that penalizes as the size of the network increases.



## Chapter 5

### Conclusions

In summary, we have presented the network dynamics derived from electrocorticographic data recorded from 15 patients who participated in a word completion task. Our approach incorporated multiple tools to evaluate the precise timing, location, and direction of information flow from the ECoG data. We extended the findings of others (Bedo et al. (2014); Mainy et al. (2008); Mechelli et al. (2005); Flinker et al. (2015)) to reveal temporally precise traces of information flow, specifically focusing on those involving fusiform. The top-down and bottom-up exchanges were realized as patients transformed visually presented, unfamiliar alphabetic strings into spoken output of familiar words.

Overall, our findings support models which allow for feedback connections to fusiform, such as the Interactive Account (Price and Devlin (2011)). We add to these models by revealing the presence of intimate, bidirectional links involving fusiform and cortex associated with higher level processing in the absence of visual input (as patients said aloud complete words in response to visually presented incomplete word stems). With the advent of network analysis tools, such as SdDTF, we stress the importance of their utilization in conjunction with other analysis technique, which enable the precise approximation of timing and location of network changes.

## Bibliography

- A Anticevic, DI Dierker, SK Gillespie, G Repovs, JG Csernansky, DC Van Essen, and DM Barch. Comparing surface-based and volume-based analyses of functional neuroimaging data in patients with schizophrenia. *NeuroImage*, 41:835–848, 2008.
- N Bedo, U Ribary, and LM Ward. Fast dynamics of cortical functional and effective connectivity during word reading. *PLoS Biology*, 9, 2014.
- JS Bendat and AG Piersol. *Random Data: Analysis and Measurement Procedures*. Wiley-Interscience, 1971.
- ALW Bokde, M Tagamets, RB Friedman, and B Horwitz. Functional interactions of the inferior frontal cortex during the processing of words and word-like stimuli. *Neuron*, 30:609–617, 2001.
- KE Bouchard, N Mesgarani, K Johnson, and EF Chang. Functional organization of human sensorimotor cortex for speech articulation. *Nature*, 495:327–332, 2013. doi: 10.1038/nature11911.
- A Brovelli, M Ding, Anders Ledberg, Y Chen, R Nakamura, and SL Bressler. Beta oscillations in a large-scale sensorimotor cortical network: Directional influences revealed by granger causality. *Proceedings of the National Academy of the Sciences*, 101:9849–9854, 2004.

- M Carreiras, BC Armstrong, M Perea, and R Frost. The what, when, where, and how of visual word recognition. *Trends in Cognitive Sciences*, 18(2):90–97, 2014.
- G Chen, ZS Saad, AR Nath, MS Beauchamp, and RW Cox. fMRI group analysis combining effect estimates and their variances. *NeuroImage*, 60:747–765, 2012.
- M Coltheart, B Curtis, P Atkins, and M Haller. Models of reading aloud: Dual-route and parallel-distributed-processing approaches. *Psychological Review*, 100(4):589–608, 1993.
- CR Conner, HZ Shouval, G Hickok, and N Tandon. Decoding the network dynamics of broca’s area and the inferior frontal convolution.
- CR Conner, G Chen, TA Pieters, and N Tandon. Category specific spatial dissociations of parallel processes underlying visual naming. *Cerebral Cortex*, 24(10):2741–2750, 2014.
- NE Crone, D Boatman, B Gordon, and L Hao. Induced electrocorticographic gamma activity during auditory perception. *Clinical Neurophysiology*, 112:565–582, 2001a.
- NE Crone, L Hao, J Hart, Jr., D Boatman, RP Lesser, R Irizarry, and B Gordon. Electrocorticographic gamma activity during word production in spoken and sign language. *Neurology*, pages 2045–2053, 2001b.
- AM Dale, B Fischl, and MI Sereno. Cortical surface-based analysis. i. segmentation and surface reconstruction. *NeuroImage*, 9:179–194, 1999.
- AR Damasio and D Tranel. Nouns and verbs are retrieved with differently distributed neural

- systems. *Proceedings of the National Academy of Sciences of the United States of America*, 90:4957–4960, 1993.
- A Daniele, L Giustolisi, MC Silveri, C Colosimo, and G Gainotti. Evidence for a possible neuroanatomical basis for lexical processing of nouns and verbs. *Neuropsychologia*, 32(11): 1325–1341, 1994.
- S Dehaene. *Reading in the Brain: The Science and Evolution of a Human Invention*. Penguin Group, 2009.
- S Dehaene and L Cohen. The unique role of the visual word form area in reading. *Trends in Cognitive Sciences*, 15(6):254–262, June 2011.
- S Dehaene, G Le Clec’H, J-B Poline, D Le Bihan, and L Cohen. The visual word form area: a prelexical representation of visual words in the fusiform gyrus. *NeuroReport*, 13(3):321–325, 2002.
- RP Dhond, RL Buckner, AM Dale, K Marinkovic, and E Halgren. Spatiotemporal maps of brain activity underlying word generation and their modification during repetition priming. *Journal of Neuroscience*, 21(10):3564–3571, 2001.
- M Ding, Y Chen, and SL Bressler. Granger causality: Basic theory and application to neuroscience. In B. Schelter, M. Winterhalder, and J. Timmer, editors, *Handbook of Time Series Analysis: Recent Theoretical Developments and Applications*, pages 437–460. WILEY-VCH, 2006.

AR Dykstra, AM Chan, BT Quinn, R Zebeda, CJ Keller, J Cormier, JR Madsen, EN Eskandar, and SS Cash. Individualized localization and cortical surface-based registration of intracranial electrodes. *NeuroImage*, 59:3563–3570, 2012.

E Edwards, SS Nagarajan, SS Dalal, RT Canolty, HE Kirsch, NM Barbaro, and RT Knight. Spatiotemporal imaging of cortical activation during verb generation and picture naming. *NeuroImage*, 50:291–301, March 2010. doi: 10.1016/j.neuroimage.2009.12.035.

TM Ellmore, MS Beauchamp, TJ O’Neill, S Dreyer, and N Tandon. Relationships between essential cortical language sites and subcortical pathways. *Journal of Neurosurgery*, 111:755–766, 2009.

F Esposito, N Singer, I Podlipksy, I Fried, T Hendler, and R Goebel. Cortex-based inter-subject analysis of iEEG and fMRI data sets: application to sustained task-related BOLD and gamma responses. *NeuroImage*, 66:457–468, 2012.

J Fiez and S Petersen. Neuroimaging studies of word reading. *Proceedings of the National Academy of Sciences of the United States of America*, 95:914–921, 1998.

A Flinker, A Korzeniewska, AY Shestyuk, PJ Franaszczuk, NF Dronkers, RT Knight, and NE Crone. Redefining the role of broca’s area in speech. *Proceedings of the National Academy of Sciences of the United States of America*, 2015.

CWJ Granger. Investigating causal relations by econometric models and cross-spectral methods. *Econometrica*, 37(3):424–438, 1969.

PJ Green and BW Silverman. *Nonparametric Regression and Generalized Linear Models: A Roughness Penalty Approach*. Chapman & Hall, 1994.

AE Hillis and A Caramazza. Representation of grammatical categories of words in the brain. *Journal of Cognitive Neuroscience*, 7(3):396–407, 1995.

K Jerbi, T Ossandon, CM Hamame, S Senova, SS Dalal, J Jung, L Minotti, O Bertrand, A Berthoz, P Kahane, and JP Lachaux. Task-related gamma-band dynamics from an intracerebral perspective: review and implications for surface EEG and MEG. *Human Brain Mapping*, 30:1758–1771, 2009.

G Jobard, F Crivello, and N Tzourio-Mazoyer. Evaluation of the dual route theory of reading: a metaanalysis of 35 neuroimaging studies. *NeuroImage*, 20:693–712, 2003.

J Joseph, K Noble, and G Eden. The neurobiological basis of reading. *Journal of Learning Disabilities*, 2001.

CM Kadipasaoglu, VG Baboyan, CR Conner, G Chen, ZS Saad, and N Tandon. Surface-based mixed effects multilevel analysis of grouped human electrocorticography. *NeuroImage*, 101:215–224, 2014.

MJ Kamiński and KJ Blinowska. A new method of the description of the information flow in the brain structures. *Biological Cybernetics*, 65:203–210, 1991.

A Korzeniewska, CM Crainiceanu, R Kuś, PJ Franaszczuk, and N Crone. Dynamics of

- event-related causality in brain electrical activity. *Human Brain Mapping*, 29:1170–1192, 2008. doi: 10.1002/hbm.20458.
- A Korzeniewska, CM Crainiceanu, R Kuś, PJ Franaszczuk, and N Crone. Dynamics of large-scale cortical interactions at high gamma frequencies during word production: Event related causality (ERC) analysis of human electrocorticography (ECoG). *NeuroImage*, 56: 2218–2237, 2011. doi: 10.1016/j.neuroimage.2011.03.030.
- JP Lachaux, N Axmacher and F Mormann, E Halgreen, and NE Crone. High-frequency neural activity and human cognition: Past, present and possible future of intracranial eeg research. *Progress in Neurobiology*, 98:279–301, 2012.
- JPh Lachaux, D Rudrauf, and P Kahane. Intracranial EEG and human brain mapping. *Journal of Physiology - Paris*, 97:613–628, 2003.
- J Levy, C Pernet, S Treserras, K Boulanouar, I Berry, F Aubry, J-F Demonet, and P Celsis. Piecemeal recruitment of left-lateralized brain areas during reading: A spatio-functional account. *NeuroImage*, 43:581–591, 2008.
- N Mainy, J Jung, M Baciú, P Kahane, B Schoendorff, L Minotti, D Hoffman, O BerO Bertrand, and J-P Lachaux. Cortical Dynamics of Word Recognition. *Human Brain Mapping*, 29:1215–1230, 2008.
- R McCarthy and EK Warrington. Phonological reading: Phenomena and paradoxes. *Cortex*, 22:359–380, 1986.

A Mechelli, JT Crinion, S Long, KJ Friston, MA Lambon Ralph, K Patterson, JL McClelland, and CJ Price. Dissociating reading processes on the basis of neuronal interactions. *Journal of Cognitive Neuroscience*, 17(11):1753–1765, 2005.

KJ Miller, EC Leuthardt, G Schalk, RP Rao, NR Anderson, DW Moran, JW Miller, and JG Ojemann. Spectral changes in cortical surface potentials during motor movement. *Journal of Neuroscience*, 27:2424–2432, 2007.

M Morf, A Vieira, DTL Lee, and T Kailath. Recursive multichannel maximum entropy spectral estimation. *IEEE Transaction on Geoscience Electronics*, GE-16(2):85–94, 1978.

AC Nobre, T Allison, and G McCarthy. Word recognition in the human inferior temporal lobe. *Nature*, 372:260–263, 1994.

JG Ojemann, RL Buckner, E Akbudak, AZ Snyder, JM Ollinger, RC McKinstry, BR Rosen, SE Petersen, ME Raichle, and TE Conturo. Functional MRI studies of word-stem completion: Reliability across laboratories and comparison to blood flow imaging with PET. *Human Brain Mapping*, 6:203–215, 1998.

NN Oosterhof, T Wiestler, PE Downing, and J Diedrichsen. A comparison of volume-based and surface-based multi-voxel pattern analysis. *NeuroImage*, 56:593–600, 2011.

K Patterson and JR Hodges. Deterioration of word meaning: Implications for reading. *Neuropsychologia*, 30(12):1025–1040, 1992.

TA Pieters, CR Conner, and N Tandon. Recursive grid partitioning on a cortical surface



- model: an optimized technique for the localization of implanted subdural electrodes. *Journal of Neurosurgery*, 118:1086–1097, May 2013.
- CJ Price. A review and synthesis of the first 20 years of PET and fMRI studies of heard speech, spoken language and reading. *NeuroImage*, 62:816–847, 2012.
- CJ Price and JT Devlin. The myth of the visual word form area. *NeuroImage*, 19:473–481, 2003.
- CJ Price and JT Devlin. The interactive account of ventral occipitotemporal contributions to reading. *Trends in Cognitive Sciences*, 15(6):246–253, June 2011.
- ZS Saad and RC Reynolds. Suma. *NeuroImage*, 62:768–773, 2012.
- NT Sahin, S Pinker, SS Cash, D Schomer, and E Halgren. Sequential processing of lexical, grammatical, and phonological information within Broca’s area. *Science*, 326(5951):445–449, October 2009. doi: 10.1126/science.1174481.
- M Schurz, M Kronbichler, J Crone, F Richlan, J Khackl, and H Wimmer. Top-down and bottom-up influences on the left ventral occipito-temporal cortex during visual word recognition: An analysis of effective connectivity. *Human Brain Mapping*, 35:1668–1680, 2014.
- MS Seidenberg. Connectionist models of word reading. *Current Directions in Psychological Science*, 14(5):238–242, 2005.
- N Tandon. Cortical mapping by electrical stimulation of subdural electrodes: language areas. In HO Lüders, editor, *Textbook of Epilepsy Surgery*. Informa UK Ltd, 2008.

JR Vidal, S Freyermuth, K Jerbi, CM Hamamé, T Ossandon, O Bertrand, L Minotti, P Kahane, A Berthoz, and JP Lachaux. Long-distance amplitude correlations in the high gamma band reveal segregation and integration within the reading network. *The Journal of Neuroscience*, 2012.

G Wahba. "confidence intervals" for the cross-validated smoothing spline. *Journal of the Royal Statistical Society. Series B*, 45(1):133–150, 1983.

G Wahba and J Wendelberger. Some new mathematical methods for variational objective analysis using splines and cross validation. *Monthly Weather Review*, 108:1122–1143, 1980.

Y Wang and G Wahba. Confidence intervals for smoothing splines and their comparison to bayesian 'confidence intervals'. Technical report, University of Wisconsin, 1210 West Dayton Street, January 1994.

EK Warrington and T Shallice. Word-form dyslexia. *Brain*, 103:99–112, 1980.

JG Wendelberger. The computation of laplacian smoothing splines with examples. Technical report, University of Wisconsin-Madison, 1981.